REVIEW ARTICLE

Generation and detection of pulsed terahertz waves in gas: from elongated plasmas to microplasmas

Fabrizio BUCCHERI[1], Pingjie HUANG[2], Xi-Cheng ZHANG (✉)[1,3]

1 The Institute of Optics, University of Rochester, Rochester, NY 14627, USA
2 State Key Laboratory of Industrial Control Technology, College of Control Science and Engineering,
Zhejiang University, Hangzhou 310027, China
3 The Beijing Advanced Innovation Center for Imaging Technology, Capital Normal University, Beijing 100037, China

Abstract The past two decades have seen an exponential growth of interest in one of the least explored region of the electromagnetic spectrum, the terahertz (THz) frequency band, ranging from to 0.1 to 10 THz. Once only the realm of astrophysicists studying the background radiation of the universe, THz waves have become little by little relevant in the most diverse fields, such as medical imaging, industrial inspection, remote sensing, fundamental science, and so on. Remarkably, THz wave radiation can be generated and detected by using ambient air as the source and the sensor. This is accomplished by creating plasma under the illumination of intense femtosecond laser fields. The integration of such a plasma source and sensor in THz time-domain techniques allows spectral measurements covering the whole THz gap (0.1 to 10 THz), further increasing the impact of this scientific tool in the study of the four states of matter.

In this review, the authors introduce a new paradigm for implementing THz plasma techniques. Specifically, we replaced the use of elongated plasmas, ranging from few mm to several cm, with sub-mm plasmas, which will be referred to as microplasmas, obtained by focusing ultrafast laser pulses with high numerical aperture optics (NA from 0.1 to 0.9).

The experimental study of the THz emission and detection from laser-induced plasmas of submillimeter size are presented. Regarding the microplasma source, one of the interesting phenomena is that the main direction of THz wave emission is almost orthogonal to the laser propagation direction, unlike that of elongated plasmas. Perhaps the most important achievement is the demonstration that laser pulse energies lower than 1 μJ are sufficient to generate measurable THz pulses from ambient air, thus reducing the required laser energy requirement of two orders of magnitude compared to the state of art. This significant decrease in the required laser energy will make plasma-based THz techniques more accessible to the scientific community, as well as opening new potential industrial applications.

Finally, experimental observations of THz radiation detection with microplasmas are also presented. As fully coherent detection was not achieved in this work, the results presented herein are to be considered a first step to understand the peculiarities involved in using the microplasma as a THz sensor.

Keywords terahertz waves, Terahertz Air Photonics, generation and detection, elongated plasmas, microplasmas

1 Introduction

Terahertz (THz) time-domain techniques, such as time-resolved THz spectroscopy (TRTS) [1] and THz time-domain spectroscopy (THz-TDS) [2], are becoming a widely used tool to study dynamics and equilibrium properties of the four states of matter [3–6].

In most studies, those techniques were implemented using solid-state THz emitters and sensors, specifically inorganic nonlinear crystals or photoconductive antennas, which limited the spectral coverage of the measurements to few THz. However, the ability to access a broader portion of the electromagnetic spectrum extending to higher frequencies is in demand. In fact, for non-equilibrium studies it allows to simultaneously access correlated dynamics associated with different excitation channels having spectral signatures in separate frequency regions. An example is given in Ref. [7], which analyzed the evolution of phonon features and electron conductivity

during a photo-induced phase transition in VO_2. Moreover, from an application standpoint, one should consider the presence of THz spectral signatures in chemicals relevant to security applications, e.g., explosives and drugs, across the entire THz gap [8,9]. Therefore, being able to cover an extended spectral range improves the confidence with which those substances can be identified by increasing the measurement window to allow the detection of more spectral "fingerprints."

The spectral coverage, or measurement window, of THz time-domain techniques can be significantly increased by using gas plasmas induced by energetic femtosecond pulses as both THz source and sensor [10–14]. Other approaches worth mentioning are the use of thin electro-optic organic polymers [15], and the very recently demonstrated use of emitters based on spintronics [16]. However, with gas plasmas there is no concern about laser-induced damage at high intensities. Moreover, gas plasmas provide a gradual refractive index interface to the THz radiation, as opposed to the abrupt interface of a solid material, therefore eliminating the spectral spatial filtering due to total internal reflection and the introduction of Fresnel reflections in the measurements.

In the majority of cases, both the generation and detection of THz radiation from gas plasma were implemented by focusing the laser field with numerical apertures (NA) smaller than 0.1 in ambient air, resulting in the creation of elongated plasma strings for which the longitudinal dimension is much greater than the transverse one. Typical lengths for those elongated plasmas range from a few millimeters to tens of centimeters.

Regarding the choice of gas to be used, it is remarkable that ambient air itself, employed as an intense THz source and ultra broadband sensor, allows the realization of spectroscopic measurements with high signal-to-noise ratio (SNR) and dynamic range [11–14,17]. Despite other gases offering improved performances in terms of generation efficiency [18] and detection sensitivity [19], ambient air is readily available, does not require the use of a gas cell, and clearly does not impose any health hazard or handling complexity.

However, the requirement for the air to be ionized together with the use of low numerical aperture focusing limited THz plasma sources to be realized with low repetition rate amplified ultrafast laser systems (with mJ pulse energies). Hence, compared to solid-state emitters, cost and complexity are moved from the THz source to the laser system. Throughout the manuscript the minimum value of laser pulse energy necessary to generate measurable THz waveforms will be referred to as the laser energy threshold. Reported values in literature for this quantity are in the range of $30 - 50$ µJ [20,21].

In this review, the use of ambient air laser-induced microplasmas as THz emitters was demonstrated and its feasibility as THz sensors was studied. For these plasmas, the laser energy threshold is reduced to the sub-µJ level

making them a viable solution to scaling down the energy requirements to implement THz plasma techniques.

2   Basic concepts

The THz frequency band can be considered one of the most elusive portions of the electromagnetic (EM) spectrum, due especially to the difficulty of developing strong sources. As a matter of fact, the universe is bathed in THz energy. According to results from the NASA Cosmic Background Explorer Diffuse Infrared Background Experiment, approximately one-half of the total luminosity and 98% of the photons emitted since the Big Bang fall into the $0.6 - 8$ THz frequency range [22]. Even the human body constantly emits THz photons as a tail of its blackbody radiation.

For a more detailed review of THz science, including the treatment of narrow band (continuous wave) THz techniques, the author strongly recommends the following review papers [23–25]. A historical review of THz radiation science is written by Prof. M. F. Kimmitt [26], which traces back the evolution of THz science to the first experiments with long wavelength radiation by Heinrich Rubens in 1893. Also recommended is the "Terahertz Pioneers" series on the *IEEE Transactions on Terahertz Science and Technology* [27–46], which is a collection of interviews given by Prof. Peter Siegel with significant contributors to THz science and technology, containing interesting anecdotes and extremely valuable information, especially for young students.

2.1   Ultrafast terahertz techniques

2.1.1   Definition of the terahertz frequency band

The International Telecommunication Union (ITU), which is the specialized agency of the United Nations responsible for matters concerning information and communication technologies, designed as "THz frequencies" the electro-magnetic waves within the band spanning from 0.3 to 3 THz. Alternative names for THz radiation commonly found in literature are: submillimeter waves, T-rays, and tremendously high frequency (THF).

2.1.2   Characteristics of terahertz radiation

The THz frequency band is located in between two spectral regions, the microwaves and the infrared radiation (as shown in Fig. 1) with mature but very different technologies and techniques that can be broadly referred to as "electronics" and "optics" respectively. During the past 30 years, both scientific communities have pushed their technologies toward each other: to higher frequencies, from the electronics/microwaves side, and to lower
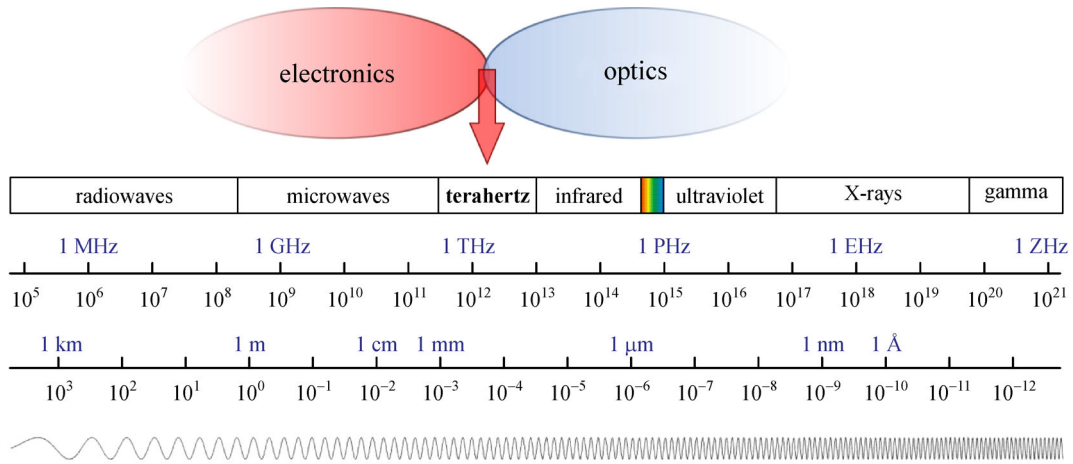
Fig. 1 Electromagnetic spectrum. The terahertz frequency band bridges electronics and optics (modified from http://www.physik.uni-kl. de/en/beigang/forschungsprojekte/)

frequencies, from the optics/infrared side. The THz frequency band, once considered a gap between those two worlds, can nowadays, after decades of intense scientific research, claim to be the "bridge" between electronics and optics.

The feature of THz radiation that attracted copious interest in this portion of the electromagnetic spectrum is the possibility to combine non-destructive imaging of concealed objects with spectral sensitivity. Which said in simpler terms: the potential to take an image of an object inside an opaque container, such as a box, a bag or a piece of clothing, and on top of that to be able to identify it through its chemical composition. More descriptions about THz wave characteristics can be seen in Refs. [47–50].

2.1.3 Generation of terahertz pulses

In this section, we will develop an understanding of the generation process of THz pulses, intended as bursts of coherent electromagnetic radiation of duration close to 1 ps and with frequency content within the THz frequency band. A typical THz pulse and its spectrum are shown in Fig. 2.

At optical frequencies, visible and near-infrared, short pulses are usually generated in laser media with large amplification bandwidth through methods known as "Q-switching" and "mode-locking" [51]. Those techniques are still not implementable at THz frequencies due to the lack of suitable materials.

THz transients can be realized in large-scale facilities like linear accelerators [52] and free-electron lasers [53], however for this paper we shall limit to discuss only "table-top" sources, i.e., systems that fit on an optical table and can be implemented in a small laboratory. Those require an ultrafast laser source (time duration < 1 ps) operating in the visible or near-infrared and a conversion mechanism from the optical frequencies to the THz range.

The generation of THz pulses has been reported for a wide range of materials, including semiconductors, metals
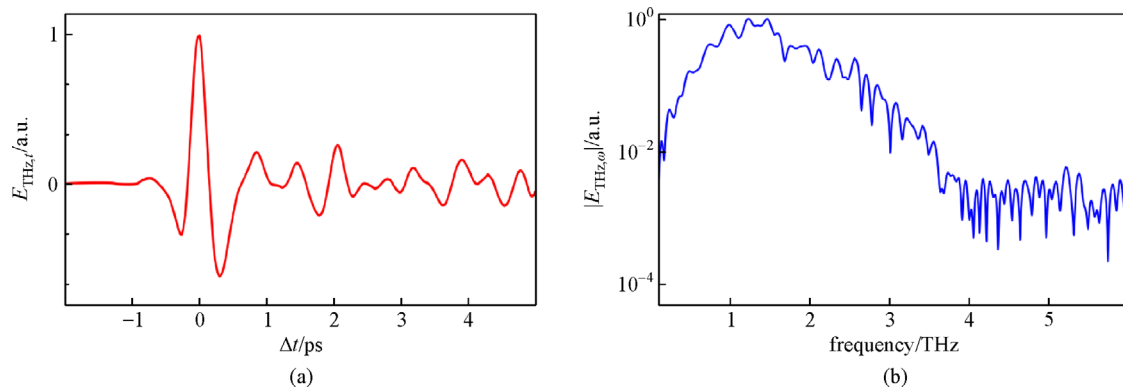
Fig. 2 Typical measured THz waveform (a) and its spectrum (b) obtained as the magnitude of its Fourier transform. The oscillatory tail after the main pulse ($\Delta t > 1$), corresponding to absorption features in the spectrum, is an effect of the propagation of the pulse through ambient air

and gases, under the illumination of femtosecond laser pulses [23,25,54,55].

The most widely used techniques to generate THz pulses are optical rectification [54–60] and photoconductive switching [61–65]. Another scheme gaining popularity in the last decade is the THz generation from ionized gases.

2.1.4   Detection of terahertz pulses

What distinguishes mainly the detection of THz radiation from the detection at optical frequencies are the much lower photon energies, in the order of few meV, involved in the former. As a result, the ambient background thermal noise is likely to be very significant or even dominate any energy associated with THz photons. This requires the use of detection techniques able to extract the signal of interest from a noise background many times larger. One of such techniques, and also the most used, is the "Phase Sensitive Detection" and it is often implemented with an instrument called "Lock-in Amplifier." This device is equivalent to an amplifier combined with an extremely narrow band filter, whose central frequency can be tuned and locked to a desired reference frequency.

The particular detectors employed for the measurement of broadband THz radiation can be classified into two categories: 1) direct and 2) coherent detectors. The first ones allow the measurement of the average power, whereas the latters give access to the instantaneous value of electric field. For the principle of direct detectors, we can see Refs. [66–71], and for the coherent detectors, it can be seen in Refs. [72–76].

In both cases, as a first approximation, the measured quantities are linearly proportional to the electric field amplitude of the THz pulse oscillation.

Compared to direct detectors, coherent sensors have some significant advantages. The most obvious one is that the wealth of information contained in a measured waveform greatly surpasses the knowledge of the radiation average power. The other one important to consider is that, since the measurement is gated by the ultrashort laser pulse, the sensitivity to the background thermal radiation is minimum. Therefore, when high repetition laser sources are employed, SNR in excess of 10000 can be achieved [77].

2.1.5   Terahertz time-domain techniques

The possibility of coherent detection of THz pulses enables two powerful techniques, which are becoming a widely used tool to study dynamics and equilibrium properties of the four states of matter [3–6]: THz time-domain spectroscopy (THz–TDS) [2] and time-resolved THz spectroscopy (TRTS) [1].

The coherent detection scheme described is inherently a spectrometer. In fact, the measured THz waveform has encoded information on all the materials that the THz pulse experiences during the propagation from the source to the detector. This information can be easily accessed by performing a Fourier analysis of the measured time-domain THz trace. THz-TDS consists in placing the sample of interest in THz beam path and acquiring a THz waveform. To isolate the contribution of the sample from those due to system, e.g., propagation of the THz pulse through air and through the source and the detector, a "reference" trace, where the sample is removed from the apparatus, is also required. Figure 3 shows a typical Fourier analysis of a sample using THz-TDS. The transfer function of the sample of interest, containing all the information to compute its refractive index real and imaginary parts, is simply obtained by performing the ratio of the sample and reference traces in the frequency domain.

The great advantage of THz-TDS is that, in spite of requiring simple and straightforward data processing of the experimental data, it allows to retrieve accurately the complex refractive index of the sample. Other spectroscopic techniques based on direct (incoherent) detection, such as Fourier transform infrared spectroscopy, in order to retrieve the complex refractive index have to rely on a convoluted numerical computation, the Kramer-Kronig analysis, which often provide results with high uncertainties.

The spectral coverage of a THz-TDS system is ultimately limited by the physical step size of the linear motor used to implement the delay line. However, this value is usually less than 1 μm and would correspond to a potential bandwidth of over 150 THz. In the majority of implementations, the spectral coverage of the system is limited to few THz by the absorption in the emitter and the detector, and by the time duration of the laser source. The spectral resolution is limited by the number of data points it is possible to acquire, therefore it is restricted by the time window of the measurement. This is eventually limited by the physical length of the linear motor stage. However, other factors that play a role are the dynamic range of the system, the presence of spurious replica of the THz pulse due to Fresnel reflections at the many interfaces in the system, and the repetition rate of the laser source. Commercial systems with time window of 200 ps usually achieve spectral resolution of few GHz.

THz-TDS is a great tool to study the properties of materials in equilibrium. However, it can be easily extended in order to study dynamics behaviors too. This is usually achieved by illuminating the sample with a pulse synchronized with the laser source aiming at initiating a change in the far-infrared absorption properties. The THz beam is employed to probe the evolution of the interaction with a sub-ps time scale. This specific technique is referred to as TRTS or optical pump/THz probe. A variation of the technique is to use the THz pulse also to induce a dynamic change in the material, i.e., THz pump-THz probe.
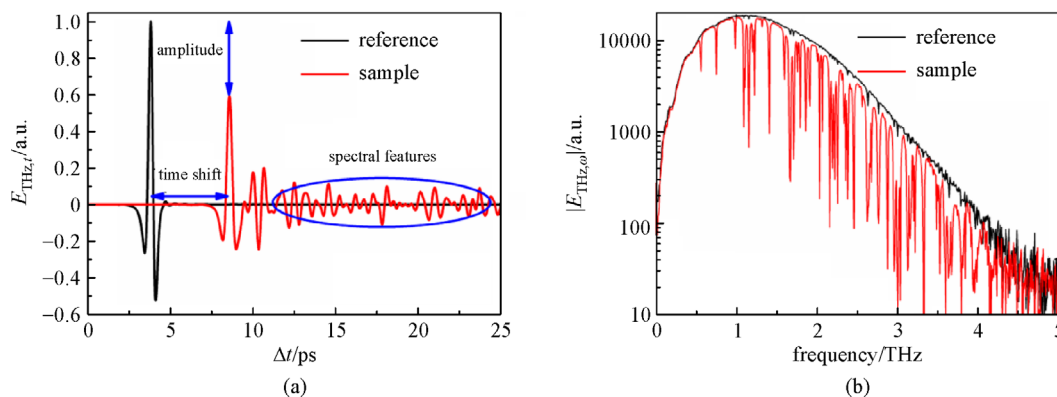
Fig. 3 Example of THz time domain spectroscopy (a). A reference trace (solid black) and a sample trace (solid red) are acquired without and with the sample inserted in the THz path respectively. Compared to the reference trace, the sample trace has: a reduced amplitude, indicating the presence of absorption; a time shift, indicating the addition in the THz path of a material with refractive index greater than one; several oscillations in its tail, indicating the presence of resonant absorption mechanisms. (b) Fourier transform of the reference and sample traces (modified from http://www.physik.uni-kl.de/en/beigang/forschungsprojekte/)

2.1.6 Applications, challenges and opportunities

1) Applications

The THz time-domain techniques described in the previous section have been increasingly employed by scientific groups spanning the whole gamut of disciplines, including chemists, physicists, biologists, and medical researchers. Moreover, it is possible to combine those with imaging and tomography [78–80], therefore resulting in images and 3D renderings of objects, where each pixel contains the spectral information of the subject.

Numerous examples of applications have been demonstrated in almost every imaginable field: skin-cancer diagnosis [81]; explosive detection [8]; verification and authentication of artwork pieces [82]; inspection of the insulation foam for the space shuttle [83]; and many others. Not to mention the contribution of THz studies to basic science advancement.

Great interest in the development of THz technologies has been always showed by the security and pharmaceutical industries. In fact, the energy of photons in the THz region allows the investigation of rotational and vibrational modes of large molecules, which are exactly the kind commonly found in compounds very relevant to those industries, such as drugs (legal and illicit), and explosives. What makes THz really attractive is that the study and identification of explosives and drugs is feasible even if the compounds are concealed in many common materials, such as clothing, paper, and plastics or in the presence of fog and smoke.

Despite the many exciting applications, at present the most impact of THz radiation has been in basic science. In fact, THz radiation allows direct observation of unique physical processes. Unlike optical waves, which mostly interacts with valence electrons, THz photons access several low-energy excitations, such as lattice vibrations, molecular rotations and spin waves [4,25,84]. Recently the development of intense table-top THz sources with peak field in excess of 1 MV/cm at frequencies below 5 THz [59,60] and 100 MV/cm between 15 and 50 THz [85] have been giving significant momentum to the study of nonlinear THz-matter interactions [86]. One of the most impressive demonstrations is the high harmonic generation from solid-state materials [87].

2) Challenges

The field of THz sciences has seen great improvements over the past decades. THz technologies are finally starting to get out from university laboratories. However, the challenges remain plenty. THz spectroscopy systems are still expensive, with the highest share of the cost due to the need for an ultrafast laser source. The high attenuation during propagation in ambient air makes applications such as communication and remote sensing very difficult to implement. Further improvements in the optical-to-THz conversion efficiency and detection sensitivity are highly desirable, and together with the development of suitable guiding structures, similarly to optical fibers, might mitigate this fundamental problem.

3) Opportunities

The THz-TDS technique has itself limitations in spectral resolution and bandwidth. To overcome those, new setup geometries need to be devised and new sources and detector need to be discovered. Many of the weaker point of THz-TDS are addressed by a technology called THz Air Photonics in next section. By using laser-induced plasmas in ambient air (or selected gases) as the THz source and sensor, the spectral bandwidth and resolution of THz-TDS system can be expanded, moreover THz remote emission and detection become possible. This technique, however,

requiring the formation of plasma, has so far demanded the use of very powerful, and therefore expensive and complicated, laser systems. This review will elaborate how a laser-induced microplasma can be used to generate and detect THz radiation with a fraction of the energy required with the conventional THz Air Photonics techniques. In addition, the microplasma add new features, and hence new opportunities for applications, to THz Air Photonics.

2.2 THz wave generation and detection in gas

Ambient air, the most readily available gas mixture on our planet, can be effectively employed to generate intense THz pulses with peak field exceeding 1 MV/cm, highly directional emission patterns and bandwidth greater than 100 THz. This can be accomplished through the process of photoionization induced by a femtosecond laser source: when a gas is illuminated by intense enough laser pulses, electrons are freed from the molecular bounds, i.e., the molecules are ionized, and plasma is created. Other than being an intense THz source, the plasma can be utilized as an ultra-broadband THz wave sensor. Techniques involving the generation and detection of THz radiation by mean of ionized air (or selected gas) are referred to THz Air Photonics.

The process of photoionization in air requires laser intensities above a critical value near 10^{13} W/cm^2. Those started to become available to scientist in the 1960s through the development of pulsed ruby and CO_2 lasers. However, due to the relatively long pulse duration of those lasers, the demonstration of the emission of THz radiation from plasma had to wait until the development of high-power femtosecond Ti:Sapphire amplified laser systems.

The first report of THz generation from ionized gas is attributed to Hamster and coworkers in 1993 [88]. In their experiment, 50 mJ near infrared pulses were tightly focused on He gas targets resulting in the measurement of sub-picosecond transients with optical to THz conversion efficiency less than 10^{-6}. This source emitted the THz radiation in a cone with large aperture angle, with no radiation in the forward direction. This technique, while simple, required very energetic laser sources and resulted in poor THz yield.

A simple approach to improve the conversion efficiency and obtain a more directional THz beam has been demonstrated by Roskos's group in 2000 [89] using ambient air as the medium. It consisted in applying an external DC bias across the laser-induced plasma. By doing so THz Air Photonics became feasible with laser energies in the order of 1 mJ, which could be obtained at much higher repetition rate, resulting in a significant increase in SNR compared to the previous technique. The major limitation of this approach was the rapid saturation of the generated THz field with increasing laser intensity and electric bias, making this technique non competitive

compared to solid states counterparts, such as large area photoconductive switch and nonlinear crystals. The saturation was caused by the poor coupling mechanism between the external DC bias, i.e., zero frequency, and the electrons in the plasma, having characteristic plasma frequencies greater than 1 THz.

Later the same year, a better way to apply an external bias to the plasma was demonstrated by Cook and Hochstrasser. Their method consisted in creating the plasma with an ultrafast laser field composed by the fundamental and its second harmonic [90]. The latter acts as an optical AC bias, allowing better transfer of energy from the laser field to the electrons in the plasma. By using this approach, conversion efficiencies of 10^{-4}–10^{-3} are routinely achieved. This method is usually referred to as "two-color" scheme, as opposed to the "one-color" scheme, in which the laser output is directly used to create the plasma. Since then, the "two-color" method became the standard one to generate intense THz pulses from ambient air.

The first demonstration of quasi-coherent detection of broadband THz radiation in ambient air has been reported in 2006 by Dai et al. [10]. Later Karpowicz et al. showed that a fully coherent detection could be implemented [11]. Recently, it has also been shown how the acoustic waves and fluorescence emitted by a laser-induced plasma allow omnidirectional and broadband detection of THz pulse [91,92]. More descriptions of one color scheme can also be seen in Refs. [88,93–98]. Further references [20,21,99–114] present more information about two color scheme.

2.3 Terahertz wave detection in gas

A gas, other than being an efficient and broadband emitter, can be successfully implemented as a versatile sensor. Several detection schemes have been demonstrated. In particular we shall distinguish two different approaches: local detection and remote detection. The first one requires the presence of measuring devices in proximity to the detection location. Currently this approach achieves the broadest useful-bandwidth and highest dynamic ranges and SNR, and it is the most suited for ultrabroadband THz-TDS measurements. The second one is implemented all optically, does not require any measuring device in proximity of the detection location, and allows omnidirectional coherent detection of THz pulses. For these reasons, it is mostly suited for remote sensing. However, characteristics such as useful-bandwidth, sensitivity, SNR and dynamic range are inferior compared to local detection.

2.3.1 Local detection: from terahertz field induced second harmonic (T-FISH) to air-biased-coherent-detection (ABCD)

For the cases of electro-optic sampling and photoconductive detection, it is often possible to reverse a THz generation mechanism in order to implement a new

detection scheme. This is also the case for the two-color generation technique. THz radiation is emitted when the fundamental beam (FB) and the second harmonic (SH) mix in the plasma. Conversely, the interaction of THz radiation and the FB in a nonlinear medium result in the generation of SH photons.

This mechanism known as THz field induced second harmonic (T-FISH) has been initially observed in amorphous silicon by Nahata and Heinz in 1998 [115]. However, due to the poor SNR compared to electro-optic sampling, their method has not been widely used. The firsts to observe T-FISH in ambient air were Dai et al. in 2006 [10].

In both amorphous silicon and air, the scientists were able to retrieve a THz waveform through a "quasi-coherent" detection mechanism. The measured SH intensity in their cases could be expressed as follow:

$$I_{2\omega} \propto |E_{2\omega}|^2 \propto \left(\chi^{(3)} I_\omega\right)^2 (E_{THz}^2 + 2E_{THz}E_{LO} + E_{LO}^2),$$

$$(1)$$

where E_{LO} is the amplitude of a background SH signal induced by the FB. The presence of E_{LO} allows homodyne detection of the THz field when its value is large enough that the first term in Eq. (1) is negligible compared to the second one. When this condition applies, the lock-in amplifier, is able to select only the second term, which has linear dependence with the THz electric field.

The coherent detection of THz radiation through T-FISH is therefore possible, although it is accompanied by several downsides: 1) the detection is coherent for low enough value of E_{THz}, and distortion of the waveform would result otherwise; 2) the technique requires the presence of a strong background, which severely limits the dynamic range of the SH detector. The solution to those concerns

has been demonstrated by Karpowicz et al. in 2008 [11] and obtained with a simple modification of the technique.

Similarly to T-FISH, SH photons can be also generated by applying an external DC electric field. When both the THz and the DC fields are applied to the nonlinear medium the resulting expression for the SH intensity is similar to Eq. (1), with the only difference that E_{LO} is replaced by E_{DC}

$$I_{2\omega} \propto |E_{2\omega}|^2 \propto \left(\chi^{(3)} I_\omega\right)^2 (E_{THz}^2 + 2E_{THz}E_{DC} + E_{DC}^2).$$

$$(2)$$

The main difference between Eqs. (1) and (2) is that, unlike E_{LO}, the phase of E_{DC} can be easily controlled. In fact, by simply switching the sign of E_{DC}, the second term in Eq. (2) is the only one to be modulated, making it possible for the lock-in amplifier to measure it. In practice, this is obtained by applying to the nonlinear medium a high voltage square wave synchronized with the laser train of pulses.

Therefore, the final expression relating the measured SH intensity and the amplitude of the THz file is the following:

$$I_{2\omega}(\tau) \propto 2\left(\chi^{(3)} I_\omega\right)^2 E_{bias}E_{THz}(t-\tau). \qquad (3)$$

This detection method is known as air-biased-coherent-detection (ABCD) and its implementation is shown in Fig. 4(a).

Unlike with the two-color generation mechanism, all the experimental evidence can be explained through a simple four-wave mixing (FWM) model. As an example, Fig. 4(b) displays the results of a systematic study in which ABCD was implemented using different gases. The figure plots the detected SH intensity as a function of the normalized third order nonlinear susceptibility $\chi^{(3)}$ of the various

(a)

(b)
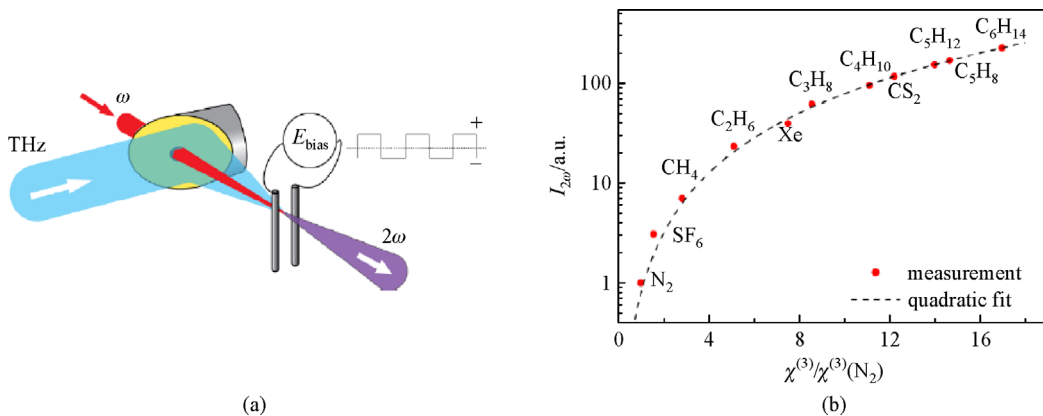
Fig. 4 (a) ABCD setup sketch: the laser probe (ω) and the THz beam are collinearly focused through two electrodes generating a signal at the second harmonic 2ω. A high voltage square wave biases the electrodes allowing the coherent measurement of THz radiation. (b) Measured second harmonic intensity as a function of the third order nonlinear susceptibility of the gas employed. All values of nonlinear susceptibility are normalized with respect to nitrogen (Reprinted with permission from Ref. [17], copyright 2012, Elsevier)

gases. The data points fit perfectly with Eq. (3). The detection sensitivity of the technique is optimized by choosing gases with large values of $\chi^{(3)}$, working at higher pressure and increasing the probe pulse energy [19].

The ABCD technique is becoming widely used due to the high performance in SNR and dynamic range. Moreover, when used in conjunction with the two-color THz generation scheme, it allows the implementation of THz-TDS systems with broad spectral range covering the whole THz band and beyond, which would be otherwise unattainable.

2.3.2 Remote detection: radiation enhanced emission of fluorescence (REEF) and terahertz enhanced acoustic (TEA)

For remote sensing applications, the main hurdle in THz science is the strong attenuation and distortion experience from a THz pulse during propagation in ambient air. Regarding the distortion, a careful study by Yang et al. showed that after traveling 167 m in ambient air a THz pulse with initial time duration of 0.5ps reshaped to a 5 ps pulse followed by rapidly oscillating tail extending to more than 150 ps [50].

Instead of sending the THz radiation toward the target and measuring the reflection off of it, this problem might be solved by implementing remote THz generation and sensing schemes. Conveniently, both fluorescence wavelengths (300–400 nm) and acoustic frequencies (10 Hz–140 kHz) benefit of little attenuation in the atmosphere, and therefore are able to carry the encoded THz fingerprint to an operator far from the target. Moreover, as both of them are emitted isotropically from the plasma, they allow the detection of broadband radiation from any direction.

1) Terahertz radiation enhanced emission of fluorescence (THz-REEF)

Among the many physical phenomena occurring in a laser-induced plasma there is fluorescence. Its origin is caused by the radiative relaxation of the free electrons liberated by the strong laser field. In ambient air, the main contribution comes from diatomic nitrogen molecules and it is located in the UV portion of the spectrum at wavelengths between 300 and 400 nm. When a THz pulse illuminates a plasma it transfers energy to the free electrons increasing their kinetic energy. As a result, those energetic electrons have the possibility to further ionize the molecules through collisional processes. The measurable interaction between the THz pulse and the plasma is an increase of the fluorescence emission intensity [91,116,117], as shown in Fig. 5.

To allow coherent detection of THz pulses, a mechanism able to distinguish the polarity of the THz field is required. This is accomplished by using a two-color laser field. In this case the net drift velocity of the ionized electrons can be controlled by the relative phase between FB and SH. In particular the net drift velocity vector can assume different orientations respect to the THz electric field vector: 1) parallel, same direction; 2) anti-parallel, opposite direction; 3) symmetric, net drift velocity is zero, i.e., the vector sum of all the free electrons velocities is zero.

In all these conditions, there is transfer of energy between the THz wave and the free electrons, however, in cases 1) and 2) electrons can be accelerated or decelerated depending on their direction of motion compared to the direction of the THz field oscillation. With this modification, the technique is sensitive to the THz field oscillation polarity and the THz waveform can be retrieved coherently by subtracting the time-resolved fluorescence curve in the parallel case from the antiparallel one (Fig. 6) [118].

This technique has been demonstrated in a full THz Air Photonics THz-TDS system, where both the emitter and sensor where implemented with laser-induced plasma, to successfully identify several explosive compounds [119]. Stand-off detection using the technique was verified by measuring THz pulses from distances up to 30 m inside the laboratory (unpublished result, Prof. Zhang's group at University of Rochester).
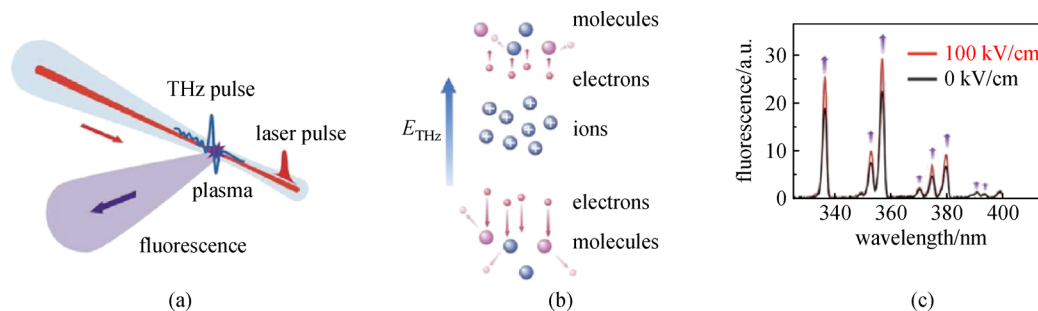
Fig. 5 (a) THz-REEF geometry. The THz pulse is focused on the plasma generated by the laser probe beam, collinearly with the laser propagation direction. The fluorescence emitted by the plasma can be collected by any angle. (b) Electrons accelerate in the THz field and collide with neighboring molecules. (c) Plasma fluorescence intensity spectrum with (red) and without (black) THz field. The fluorescence lines are all equally enhanced. (Reprinted with permission from Ref. [116], copyright 2011, IEEE)
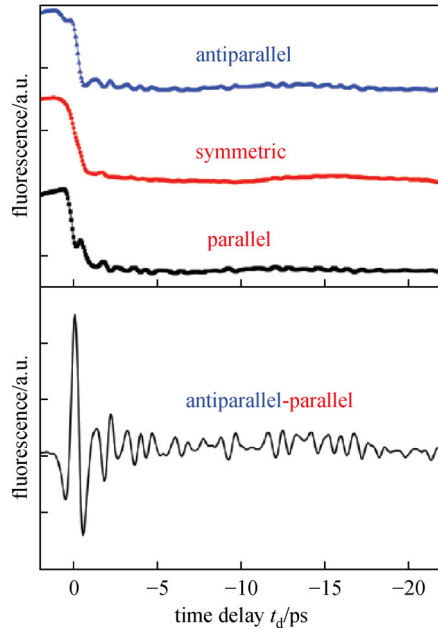
Fig. 6 (Top) Time resolved plasma fluorescence intensity for the cases of antiparallel (blue), symmetric (red) and parallel (black) electron drift velocities. (Bottom) The subtraction of the parallel trace from the antiparallel one reveals the THz waveform (Reprinted with permission from Ref. [17], copyright 2012, Elsevier)

2) Terahertz enhanced acoustics (TEA)

Other than emitting light, a laser-induced plasma produces sound. This can clearly be heard in the laboratory by the human hears as its main components occurs at the repetition rate of the laser, which usually is in the low kHz range. Together with this audible component, a broader spectrum, ranging from few Hz to almost 1 MHz, is emitted as well.

We already discussed how the THz pulse accelerates the free electrons in the plasma and increases their kinetic energy. This results in a rise of gas temperature due to the higher number of electron-electron, electron-ion, and electron-neutral atom collisions, which in turn change its pressure affecting the emission of sound. The enhancement of the acoustic emission of the plasma following the interaction with the THz wave is depicted in Fig. 7 together with a schematic of the detection geometry. Similarly to THz-REEF, in order to achieve coherent detection a two-color laser field is needed. From a setup point of view, the only difference between THz-REEF and TEA is the detector. The first one employs a UV sensitive detector, such as a photo multiplier tube (PMT), while the latter uses a microphone.

3) Comparison between THz-REEF and TEA

Currently THz-REEF offers better SNR and dynamic range compared to TEA. This is due by the stronger influence of the THz pulse on the fluorescence rather than on the sound. Also the devices available for the detection of light are more sensitive compared to those available for sounds.

Nonetheless, TEA offers very interesting advantages: 1) acoustic measurements do not require a direct line of sight, and are reflected or transmitted by more materials compared to UV light; 2) the pressure attenuation scales as $1/r$ with radial distance, while light intensity scales as $1/r^2$. Therefore, while in the laboratory THz-REEF offers a better detection technique, in the field TEA has some peculiarities that might make it prevail.

2.3.3   Challenges and opportunities

THz Air photonics allows to significantly increase the spectral coverage of THz time-domain techniques improving the impact of THz science. Moreover, due to the possibility to generate and detect THz radiation coherently and remotely, it provides an opportunity to develop exciting and much needed applications, such as stand-off sensing.
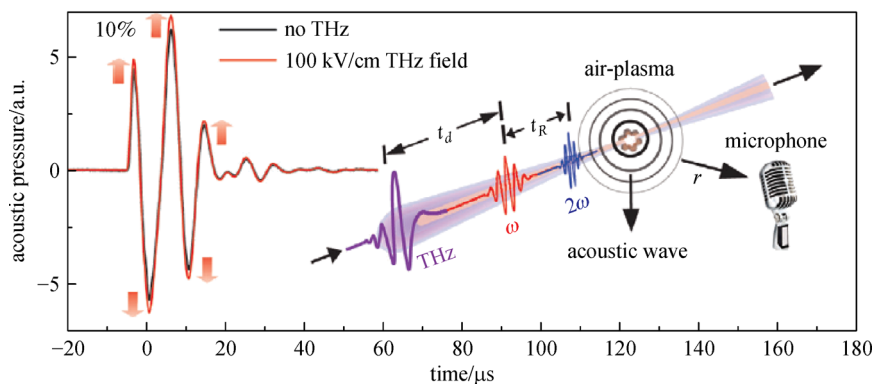
Fig. 7 Acoustic plasma emission measured with a high frequency microphone placed 10 mm away from the plasma with (red) and without (black) THz illumination. The inset shows the setup for THz Enhanced Acoustics measurements (Reprinted with permission from Ref. [17], copyright 2012, Elsevier)

While promising, THz Air Photonics faces many challenges that hinder its widespread use.

Table 1 provides an overview of the advantages and limitations of THz Air Photonics.

2.4 From elongated plasma to microplasma

One of the big challenges to transfer all the potential benefits of THz Air Photonics discussed above to real-life applications is the requirement for energetic laser systems. As the pulse energy of such lasers directly correlates with their complexity, need of specialized operator, cost and user safety concerns, strategies must be devised in order to implement THz Air Photonics with lower laser energies.

Energetic pulses are needed in order to reach intensities high enough to ionize ambient air. Those have been usually achieved by focusing high power lasers with low numerical aperture optics (NA < 0.1). However, considering that the laser intensity is not only a function of laser energy, but also of spot size, it is possible to achieve high laser intensities with significantly lower laser energies by increasing the NA of the focusing optics. By using NA greater than 0.1, air ionization is achieved with few μJ of laser energy for pulses of 100 fs duration.

The differences between plasmas generated by low and high NA optics are substantial. The most obvious one is the length of the plasma, defined as the full width half maximum (FWHM) of the electron density distribution along the laser propagation direction. In the rest of the manuscript, we will refer to plasmas with length longer than 1 mm as "elongated plasmas," with length smaller than 1 mm as "microplasmas."

Laser induced ionization processes, principles of self-focusing, plasma defocusing and intensity clamping, and effects of external focusing can be seen in Refs. [120–132]. When using intense femtosecond pulses, plasma is achieved through the processes of multiphoton and tunneling ionizations. The first one is the most likely path at lower laser intensities, while the latter at higher ones. The size of the plasma depends on the laser intensity, but mostly on the NA of the laser beam. Loosely focused laser beams will result in elongated plasmas, where the longitudinal dimension, i.e., length, is significantly longer then the transverse one, i.e., width. Sufficiently powerful and loosely focused laser beam can generate laser filaments, in which nonlinear propagation effects together with plasma defocusing create very long (tenths of centimeters to meters) plasma channels in the wake of the laser pulse. Microplasmas are obtained when the laser beam is tightly focused. Those have comparable longitudinal and transverse dimension, with values less than 1 mm. Elongated plasmas resemble a cigar in shape, while microplasmas resemble more of a sphere.

Elongated plasmas are usually characterized by lower laser intensities and plasma densities compared to microplasmas even when higher laser energies are employed. Finally, when increasing the laser energy the shape and position of the plasma tend to change in the elongated case, since those are dictated by the balance between self-focusing, external focusing and plasma defocusing. In the microplasma case, this does not happen as self-focusing is negligible. When the laser energy increases, the plasma volume grows, but the position does not change.

The comparison between elongated plasmas and microplasmas is summarized in Table 2.

3 Generation of terahertz radiation from microplasma

The use of ambient air laser-induced microplasmas as THz emitters is demonstrated. For these sources, the laser energy threshold is reduced to the sub-μJ level. Other features of interest are that the THz waves are radiated almost orthogonally to the laser propagation direction, and that the generation volume is sub-wavelength compared to the emission wavelength (1 THz = 300 μm).

3.1 One-color scheme

The experimental setup implemented THz time-resolved detection and it is schematically shown in Fig. 8. The laser excitation, provided by a commercial Ti:Sapphire amplified laser (100 fs pulse duration, 700 μJ pulse energy, 800 nm central wavelength, 1 kHz repetition rate), was split into two beams with controllable time delay (not shown in the figure).

The pump beam was focused by a 0.85 NA air

Table 1 Advantages and disadvantages of THz Air photonics

advantages	disadvantages
can be implemented with ambient air	amplified laser systems, expensive and bulky, are required (laser threshold)
useful bandwidths (> 60 THz)	low optical-to THz conversion efficiency
high peak electric fields (> MV/cm)	intense optical radiation requires higher safety standards and poses hazard
no damage threshold	low detection sensitivity
remote operation	critical alignment is required
higher spectral resolution (no Fresnel reflections)	
no absorption features	

Table 2 Comparison between elongated plasma and microplasma

microplasma	elongated plasma
length: < 1 mm	length: few mm up to meters
width: < 1 mm	width: ~ 100 µm
tight focusing of the laser (NA > 0.1)	loose focusing of the laser (NA $<< 0.1$)
higher peak laser intensity ($> 5 \times 10^{14}$ W/cm^2)	lower peak laser intensity ($\sim 1 \times 10^{14}$ W/cm^2 [20])
higher peak electron densities ($\sim 10^{18}-10^{19}$ cm^{-3})	lower peak electron densities ($\sim 10^{15}-10^{16}$ cm^{-3})
position does not change with laser energy	position changes with laser energy
lower laser energy threshold (< 1 µJ)	higher laser energy threshold ($\sim 30-50$ µJ)
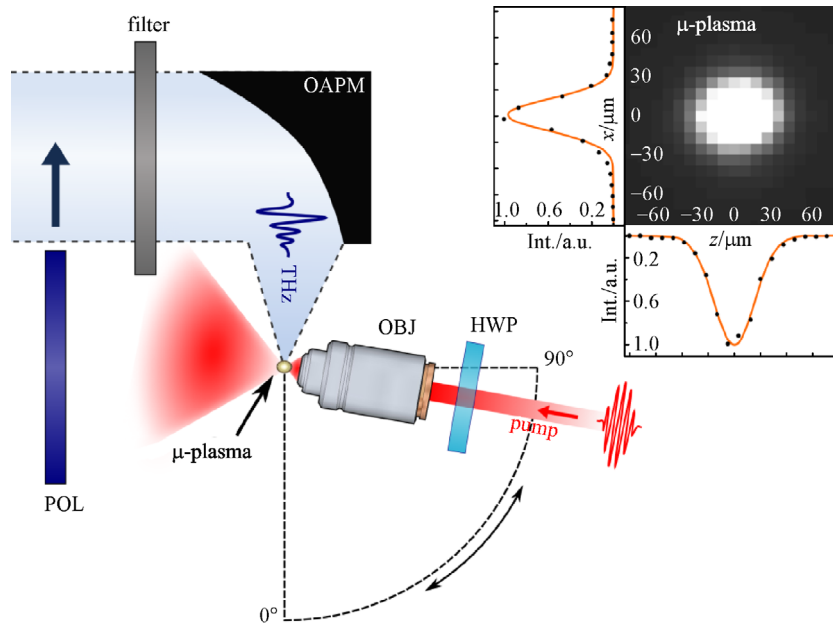
Fig. 8 THz waves are emitted by the ambient air microplasma obtained by focusing the laser excitation through a high NA objective. A high resistivity silicon wafer (filter) is inserted in the THz path in order to block the pump beam. The waveforms are retrieved with electro-optic sampling. The THz generation portion of the setup can be rotated about the position of the microplasma in order to study the angle-dependent emission from the source. The inset is a picture of the microplasma created by focusing laser pulses with energy of 65 µJ through a 0.85 NA air-immersion objective as seen through a UV bandpass filter. The laser excitation propagates from right to left. The plasma is imaged from the side with a commercial iCCD camera. The fluorescence profile is Gaussian. The FWHM for the longitudinal and the transverse fluorescence intensity profile is (36.7±8.7) µm and (28.5±8.7) µm respectively. List of abbreviations: HWP, half wave plate; OBJ, objective; OAPM, off-axis parabolic mirror; POL, THz polarizer

immersion microscope objective into ambient air, creating a sub-mm plasma. The polarization of the pump beam was linear and its orientation could be rotated through a half wave plate. The maximum pump pulse energy employed in the experiment was 65 µJ, limited by the damage threshold of the objective. For this excitation energy, we obtained plasmas with both longitudinal and transverse sizes less than 40 µm (Fig. 8 inset). THz field resolved traces were obtained through free-space electro-optic sampling [74], where we employed a 1 mm-thick $\langle 110 \rangle$ -cut ZnTe crystal as the detector.

Our findings are illustrated in Fig. 9. We measured THz waveforms for ten different detection angles, defined as the angle between the propagation axis of the pump beam and the optical axis of the THz collecting mirror, ranging from 0° to 90°. The solid angle of collection was limited by the diameter of the first off-axis parabolic mirror for all detection angles. Figure 9(a) shows the time-resolved field measurements, while Fig. 9(b) (solid line) depicts the collected THz pulse energy, extracted from the field measurements, as a function of detection angle. In our experimental conditions, the coherent emission of THz collected in the forward direction, 0°, is negligible compared to the one collected for detection angles close to 90°. Specifically, we observed the peak of THz emission to occur around 80°.

A typical THz waveform measured for this value of detection angle for laser pulse energy of 65 µJ is shown in
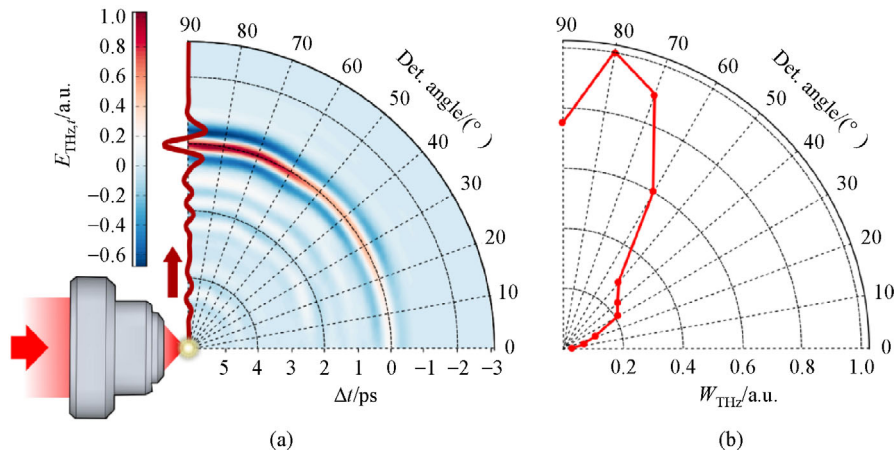
Fig. 9 (a) Density plot representing the coherent angle-dependent emission from a microplasma generated with laser pulse energy of 65 μJ. The plot is obtained through spline interpolation of ten THz waveforms recorded at different detection angles in 10° intervals starting from 0°. Each waveform is normalized to the highest value of THz field recorded in the set. Δt is the time delay between the pump and the probe beam. (b) THz pulse energy as a function of detection angle. The pulse energy is extracted from the THz waveforms displayed in (a)

Fig. 10 (top waveform). The detected spectrum is broadband and it is limited by the useful detection bandwidth, which is related to the electro-optic crystal thickness and phonon resonances. This is shown in Fig. 11(a), which demonstrates how the detected spectrum increases as the detector length decreases. Figure 11(b) illustrates that, within the capabilities of our detection technique, the measured THz spectra do not change with detection angle.

The authors also report the measurement of THz emission from ambient air excited with sub-μJ laser pulse energies. For these low levels of energy, there was not any measurable fluorescence emission from the microplasma using the iCCD camera. Figure 10 shows a THz waveform recorded for pump energy as low as 660 nJ (bottom waveform). This value is more than one order of

magnitude lower than previously reported ones [20,21] and it is limited by the SNR of the detection system.

A simple strategy to improve the SNR significantly is to use laser sources with higher repetition rate, resulting in an increased number of measured pulses in the unit of time. Commercial amplified laser systems with pulse energies of few μJ typically have repetition rates in the order of 200 – 300 kHz, which is an increase of two orders of magnitude compared to the repetition rate of our laser system. Considering that the SNR is expected to grow as the square root of the repetition rate, by employing this class of sources it is expected for the SNR to be improved by more than one order of magnitude, and THz transients to be measured with even lower pulse energies.

The measured THz emission pattern, amplitude and phase are not sensitive to linear polarization rotations of the optical pump. This is shown for the peak amplitude of the THz waveform in Fig. 12. The effect of the polarization of the laser beam was further investigated by creating more complicated polarization states, including circular (homogeneous polarization with Gaussian beam profile), optical vortex with topical charge l = 1 (homogeneous polarization with donut beam profile), and radial and azimuthal (inhomogeneous polarizations with a donut beam profile). Those polarization states are obtained by replacing the HWP (see Fig. 8) with the appropriate polarization optics: a quarter wave plate to obtain the circular polarization and a special component called "s-waveplate" to obtain the radial, azimuthal and vortex states. The results of this investigation are presented in Fig. 13, in which the waveforms obtained at 80°, maximum emission angle in all cases, are compared. The variation in peak amplitude between the linear and circular case is minimum, well within the uncertainty of the measurement. The radial,
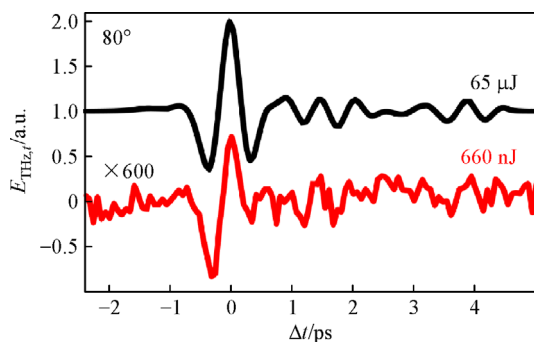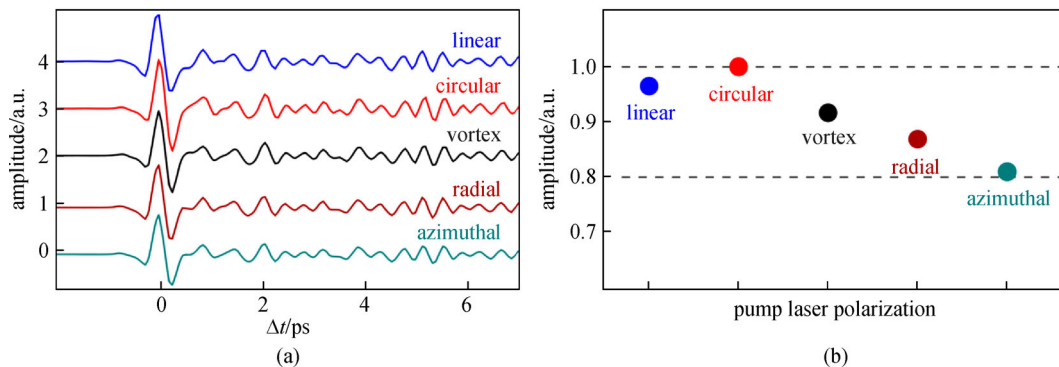

Fig. 10 Measured THz waveforms at detection angle of 80 degrees for a laser pulse energy of 65 μJ (top) and of 660 nJ (bottom). For clarity, the plots are offset and the waveform measured at 660 nJ is magnified 600 times
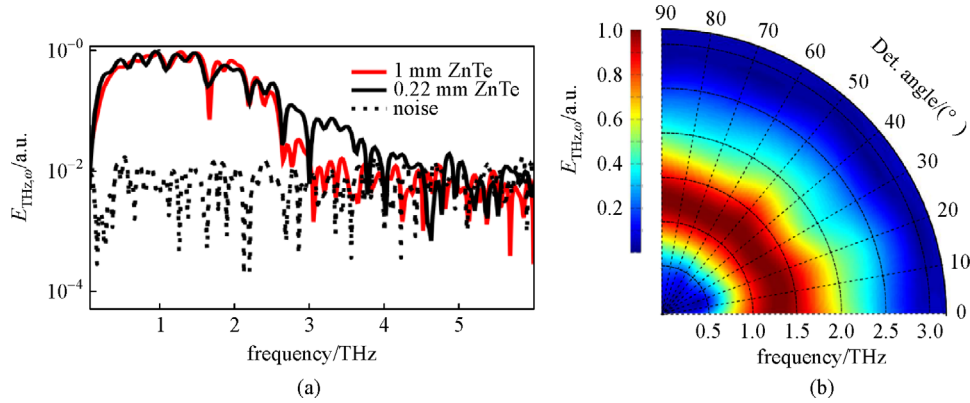
Fig. 11 (a) Measured THz spectral amplitudes with ⟨110⟩-cut ZnTe crystals of different thicknesses: 1 mm (red curve), 0.22 mm (black curve). The black dashed curve is the measured experimental noise. (b) Density plot representing the angle-dependent spectral emission from a microplasma generated with laser pulse energy of 65 μJ. The plot is obtained through spline interpolation of the Fourier transform of ten THz waveforms recorded at different detection angles in 10° intervals starting from 0°. All the spectra are normalized to one to show how the spectrum does not change appreciably with detection angle. However, by doing so the reader could be lead to believe that there is a strong emission for detection angle close to 0°. This is not the case as the amplitude of the spectra measured at 0° and 10° are more than one order of magnitude lower than those measured at larger angles
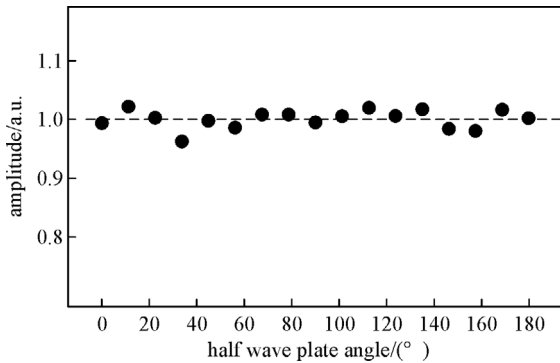
Fig. 12 Peak amplitude of measured THz waveforms as a function of the azimuthal angle HWP placed in the laser beam path right before the microscope objective. The amplitude does not change upon linear rotations of the laser polarization

azimuthal and vortex beams have reduced amplitudes, close to 20% decrease for the azimuthal case, which is attributed to the donut intensity profile.

The polarization of the detected THz radiation has been investigated by inserting a wire grid polarizer in the THz path, see Fig. 8, and exploiting the inherent polarization sensitivity of electro-optic sampling similarly to Ref. [133]. THz radiation within our collection angle was horizontally polarized independently of the pump beam polarization, see Fig. 14. Due to the cylindrical symmetry of the generation mechanism, this implies that the THz emission is locally linearly polarized, and oscillating in the plane defined by the laser excitation propagation axis and the local THz propagation axis.

The THz peak power scales with the square of the pump pulse energy, as shown in Fig. 15, independently of detection angle. For pump pulse energies above 55 μJ, the experimental data starts to deviate from the parabolic fit
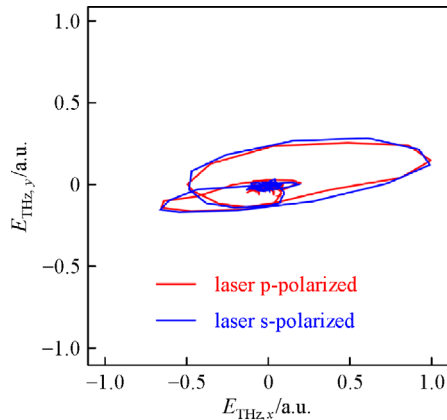

Fig. 13 (a) THz waveforms measured when the laser beam has the following polarizations: linear (blue), circular (red), vortex (black), radial (magenta), azimuthal (green). (b) Comparison of the peak amplitudes obtained in the cases mentioned above

Fig. 14 Parametric plot representing the measured polarization of the THz radiation in the case of p-polarized (red) and s-polarized (blue) laser beam. The polarization state of the collected THz wave does not change with the polarization of the laser beam

(Fig. 15(a)). Rather than to the saturation of the emission mechanism, this was attributed to the onset of nonlinear interactions between the intense laser pulse and the glass composing the objective, such as self-phase modulation. In fact, for pulse energies at which saturation occurred, white light generation inside the objective was visible by naked eye. In a separate experiment, the THz emission was shown to saturate at much higher pump pulse energies. The setup was very similar to the one shown in Fig. 8, with the exception of the laser source, which was more energetic and offered a shorter pulse duration (800 nm, 50 fs, 3.5 mJ, 1 kHz), and the focusing element. Specifically the 0.85 NA microscope objective was replaced by a 0.77 NA aspheric lens, which is able to sustain much higher laser fluences compared to the objective. The dependence on laser energy of the THz peak power shows saturation at energies close to 250 μJ, much higher than those obtained with the microscope objective (Fig. 15(b)). While the THz emission

saturates, above those energies the plasma fluorescence intensity keeps growing quadratically suggesting that the saturation does not originate from depletion of neutral atoms in the focal volume. Instead, the likely mechanism is the decreased penetration depth of the THz radiation in the plasma due to the increased electron density, which prevents the THz emission from the densest part of the plasma to couple out.

Using the 50 fs laser source, the emission pattern of microplasmas of three different sizes was measured. The microplasmas were obtained by focusing the optical pulses with aspheric lenses with same clear aperture, but different effective focal length, i.e., NA. Specifically, the author measured the angular dependence of the radiated THz wave with electro-optic sampling of microplasmas with lengths of 72, 78, 120 μm obtained with numerical apertures of 0.77 NA, 0.68 NA, and 0.40 NA respectively. At the same energy level of 200 μJ, below the onset of saturation for each of the three cases, the THz emission was stronger for tightest focusing case, i.e., highest NA. As the plasma length increases, the angle at which the peak of radiation occurs moves toward the laser propagation axis. Those results are visually depicted in Fig. 16 and summarized in Table 3.

The efficiency of the generation process was estimated by calibrating the waveform obtained with electro-optic detection [60]. The highest optical-to-THz conversion efficiency was of $\sim 3 \times 10^{-6}$ and was obtained with the 100 fs laser and the 0.85 NA microscope objective. Despite the much higher energies employed with the aspheric lenses, the conversion efficiencies were in the order of $\sim 2 \times 10^{-7}$. Evidently the reduced laser pulse time duration, 50 fs vs. 100 fs, must play an important role. It is important to note that those values of conversion efficiencies are to be intended as laser energy-to-THz energy at the detector. In the microplasma case, this subtlety is relevant as the collection solid angle is significantly smaller than the
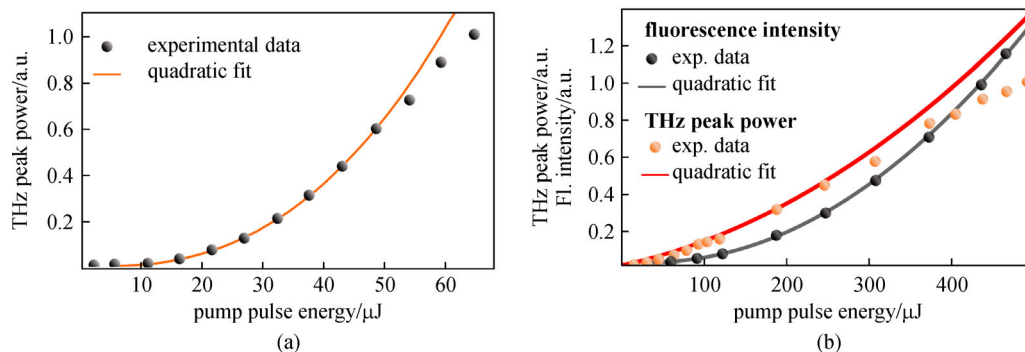
Fig. 15 (a) THz peak power as a function of laser pulse energy for a detection angle of 80°. The laser source is Spectra Physics Hurricane (800 nm, 100 fs, 0.7 mJ, 1 kHz) and the microplasma is created with the 0.85 NA microscope objective. The dots are the experimental data, while the solid line is a quadratic fit. (b) THz peak power as a function of laser pulse energy for a detection angle of 80° (red). Fluorescence intensity integrated from 200 to 1000 nm as a function of laser pulse energy (gray).The laser source is Coherent Libra (800 nm, 50 fs, 50 fs, 1 kHz) and the microplasma is created with the 0.77 NA aspheric lens. The dots are the experimental data, while the solid line is a quadratic fit
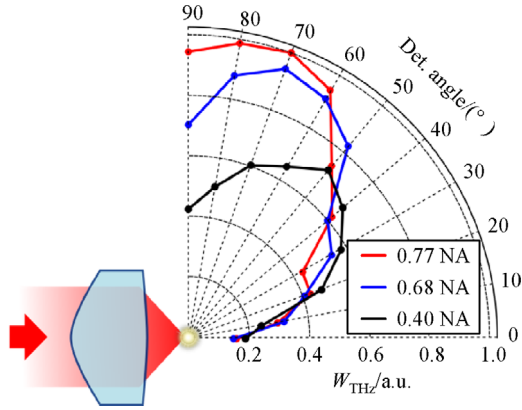
Fig. 16 THz pulse energy as a function of detection angle for microplasmas obtained with three different achromatic lenses: 0.77 NA (red); 0.68 NA (blue); 0.40 NA (black)

Table 3 Summary of the measurements of THz emission from microplasmas obtained with different focusing NA

	plasma length /μm	peak emission angle/(°)	relative peak energy (normalized)
0.77 NA	72±8.3	70	1
0.68 NA	78±8.3	70	0.93
0.40 NA	120±8.3	50	0.74

emission one, thus most of the radiated THz energy is lost. It follows that a simple way to increase the efficiency of the system is to improve the detection collection geometry. This can be achieved by placing the microplasma at the focus of a full parabolic reflector as shown in Fig. 17(a). An important thing to notice is that the polarization of the collimated THz field is radial (Figs. 17(b) and 17(c)), therefore, in the case of perfect alignment, the transverse component of the electric fields at the detector position would cancel while the longitudinal components would add up. Nonetheless, even with a detector sensitive only to the transverse components of the electric field, such as the $\langle 110 \rangle$-cut ZnTe employed in all the presented experiments, by carefully "misaligning" the parabola and tilting the detector crystal it is possible to measure stronger peak electric field at the detector compared to the cases without the parabola. In particular, the peak electric field obtained with the parabola was three times higher than the best peak electric field obtained by collecting the THz radiation with the off axis parabolic mirror.

In this optimized case, the optical-to-detected THz conversion efficiency was higher than 10^{-5}. For low laser energies, this value is better than that obtainable with elongated plasmas in the two-color approach. Figure 18 shows the comparison of the optimized THz waveforms obtained at the same laser energy of 65 μJ by one-color and two-color elongated plasmas and by microplasmas, collected with off-axis parabolic mirror and full parabola. The elongated plasmas, with length of 2 mm, were created
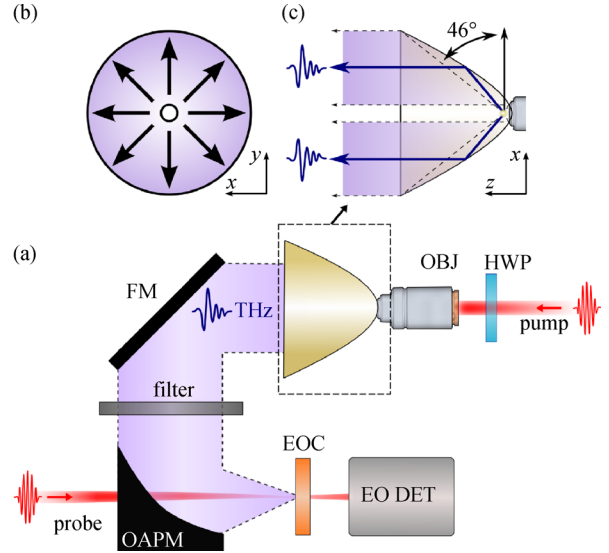
Fig. 17 (a) Experimental setup employing a parabolic reflector for the collection of the THz radiation emitted from the microplasma. (b) Diagram showing the transverse profile of the collimated THz beam exiting the parabolic reflector. The beam is radially polarized. (c) Zoom on the inside of the parabolic reflector showing how the THz radiation is collected. List of abbreviations: HWP, half wave plate; OBJ, objective; FM, flat mirror, OAPM, off-axis parabolic mirror; EOC, electro-optic crystal; EO DET, electro-optic detection
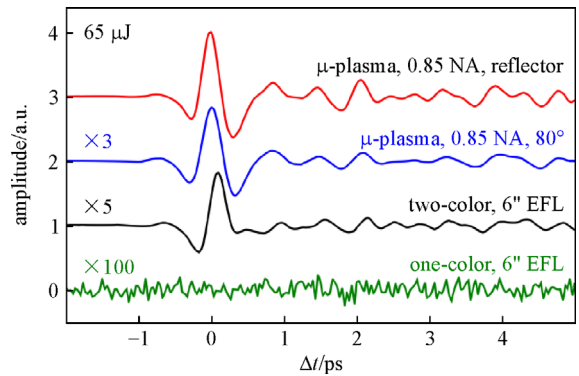
Fig. 18 Comparison of THz waveforms obtained with a laser energy of 65 μJ with the following generation schemes: microplasma collected with the parabolic reflector (red); microplasma collected with the off-axis parabolic mirror (blue); two-color elongated plasma (black); one-color elongated plasma (green)

by focusing the laser with a 6 inch effective focal length (EFL) lens. For this low value of laser energy, the microplasma offers peak THz field up to five times higher compared to the two-color elongated case. In the case of elongated one-color plasma, the THz emission is so small that is below the sensitivity of the detection.

Finally, it is instructive to compare the spectra obtained

with the microplasma and the two elongated plasmas at the laser energy at which the peak amplitude of the THz waveforms in the different configuration is the same. Those values are 214 and 102 μJ for the one-color and two-color case respectively. By doing so, one assures that the SNR of the measurement does not affect the comparison.

Compared to the one obtained with the one-color microplasma, the spectrum obtained from the elongated two-color plasma is visibly broader (Fig. 19(a)), while the one generated by the elongated one-color plasma is an almost perfect replica (Fig. 19(b)). This suggests the similarity of the generation mechanism for both micro-plasma and elongated plasma in the one-color case, and highlights the difference with the two-color technique, in which highly nonlinear mixing processes lead a broader spectrum.

3.2   Two-color scheme

To study the two-color approach using microplasmas, the setup shown in Fig. 8 had to be modified. In fact, the microscope objective employed in the previous section would introduce chromatic aberrations and dispersion between the FB and SH hindering their spatial and temporal overlap at the microplasma. For this reason, the refractive objective was replaced by a reflective objective (Schwarzschild design, 0.45 NA).

The collimated laser beam from Spectra Physics Hurricane (800 nm, 100 fs, 0.7 mJ, 1 kHz) is sent through a 1 mm-thick type I β barium borate (β-BBO). The azimuthal angle of the crystal can be rotated to maximize the SH emission, with conversion efficiencies ~ 5%. This low value of conversion efficiency is due to the fact that the laser beam had to be expanded from 5 mm to 1 cm FWHM in order to fill completely the clear aperture of the objective. The FB and SH then enters the objective and are focused to a tight spot creating a microplasma. The relative phase between FB and SH was controlled by changing the distance from the β-BBO to the microplasma through a motorized linear stage. The sketch of the generation

portion of the setup is shown in Fig. 20, while the detection part is the same as the one presented in Section 3.1 and shown in Fig. 8.

The energy losses through the objective are substantial, due to the central obscuration caused by the presence of the primary mirror and the impossibility for the secondary mirror to collect the portion of the input beam close to the optical axis, i.e., the central part, which is also the most energetic. In this experimental condition losses close to ~ 80% were measured resulting in a maximum obtainable energy at the plasma location of 90 μJ. Moreover, the beam exiting the objective has no longer a Gaussian intensity profile, but one resembling a donut (Fig. 21). Close to the objective, the beam profile presents also features due to diffraction from the holders and the edges of the primary mirror. Those are visible in Fig. 21 for distances as close as 2 mm from the focal plane of the objective. Eventually the beam collapses in a tight spot with on-axis peak intensity.

The obtained plasma length at 90 μJ was of (36±8.2) μm, very similar to that obtained with 65 μJ and the 0.85 NA objective.

The emission pattern was characterized by measuring THz waveforms for ten different detection angles ranging from 0° to 90°. The detection angle is defined as the angle between the optical axis of the THz collecting mirror and the propagation axis of the laser excitation beam. A detection angle of 0° corresponds to a direction parallel the laser beam propagation axis.

For each detection angle, a THz waveform for two different values of β-BBO azimuthal angle, α, was acquired. For α equals to 0°, i.e., crystal's ordinary axis parallel to the excitation laser polarization, the efficiency of the SH generation process is negligible, therefore this corresponds to the "one-color" case. For the "two-color" case, α equals to 48° was employed, being the value at which the THz peak electric field is the highest, despite the SH generation efficiency is maximum for a value of α equals to 90°. This occurrence is well understood and reported in Refs. [99,106]. The distance of the β-BBO crystal from the microplasma, i.e., the relative phase
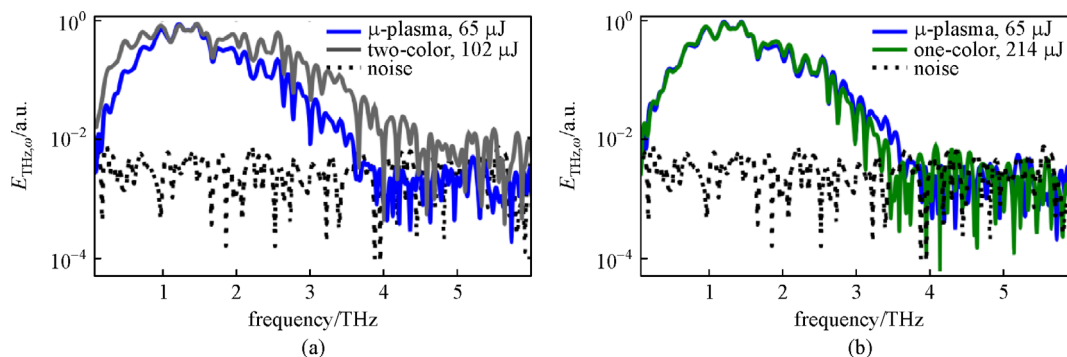

Fig. 19   (a) Comparison of the spectrum obtained with a microplasma generated with 65 μJ laser energy (blue) with two-color elongated plasma generated with 102 μJ laser energy (gray). (b) Comparison of the spectrum obtained with a microplasma generated with 65 μJ laser energy (blue) with one-color elongated plasma generated with 214 μJ laser energy (green)
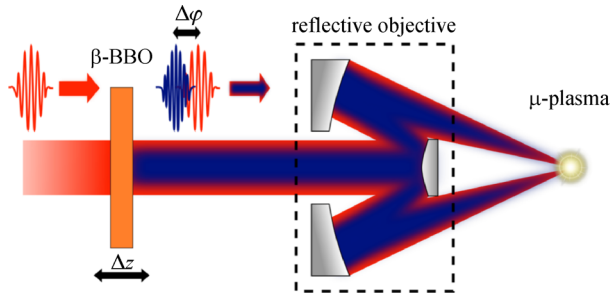
Fig. 20 Experimental arrangement for the generation of the two-color microplasma
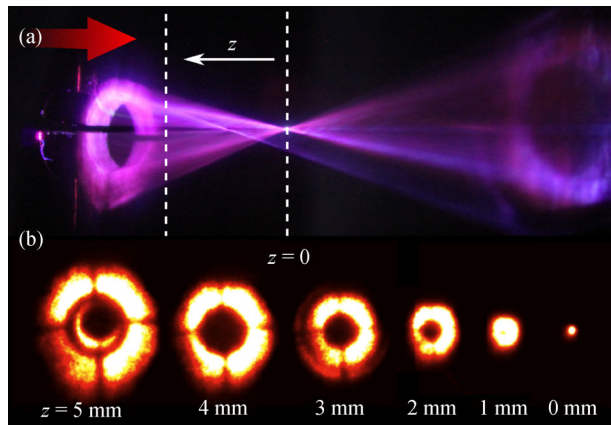
Fig. 21 (a) Visible picture of the conical laser beam exiting the reflecting objective. The laser travels from left to right. The picture is obtained with a long exposure and by slowly moving a lens tissue along the laser propagation axis so to scatter light into the camera. (b) Transverse beam profile of the laser beam captured by a CCD camera at different distances from the focal plane $z = 0$
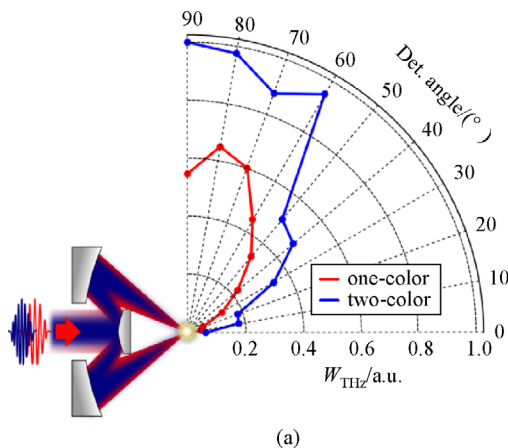
between the fundamental beam and its SH, is chosen such that the THz peak electric field is maximum.

Figure 22(a) shows the comparison between the angle-dependent emission from microplasmas induced by a one-color laser field (solid red plot) and a two-color laser field (solid blue plot) with same laser energy. Each point represents the THz pulse energy, computed as the time integral of the absolute square of the measured THz waveforms.

The presence of the SH increases the THz emission for all the considered detection angles. The highest energy enhancement is obtained in the forward direction and it is close to 300%, due to the almost negligible THz emission from the one-color microplasma in that direction. Remarkably, an unexpected significant enhancement of 47% is present for a detection angle of 90° (Fig. 22(b)).

The fact that the signal increase is due to the presence of the SH was confirmed by observing the occurrence of the signature sinusoidal modulation of the THz peak electric field as a function of the relative phase delay between the fundamental beam and the SH [21,99,105,106], as shown in Fig. 23(a). The modulation of the THz peak electric field was observed for all the values of detection angle. However, the measured modulation depth, defined as the difference between maximum and minimum value of the normalized THz peak electric field changes as a function of the detection angle. Larger modulations are obtained for detection angle in the range from 30° to 70°, while they are significantly smaller at the very large detection angles.

Figures 23(b), 23(c) and 23(d) which depict the measured modulation of the THz peak field for detection angles of 90°, 60° and 30° respectively, illustrating how the sinusoidal oscillation is not centered around zero but it is super imposed to the signal level due to the one-color
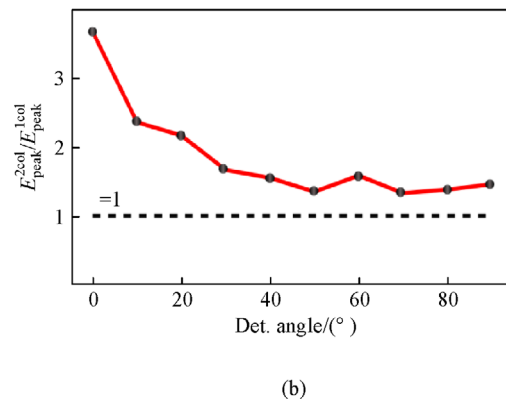
Fig. 22 (a) THz pulse energy as a function of detection angle in the one-color (red) and two-color (blue) cases. In the one-color case the azimuthal angle of the β-BBO crystal is rotated so to minimize the SH emission, while in the two-color case so to maximize the THz wave emission. (b) Ratio of the THz peak fields in the two-color and one-color case as a function of detection angle (red). The dashed black line signaling a ratio equals to one is inserted as a reference
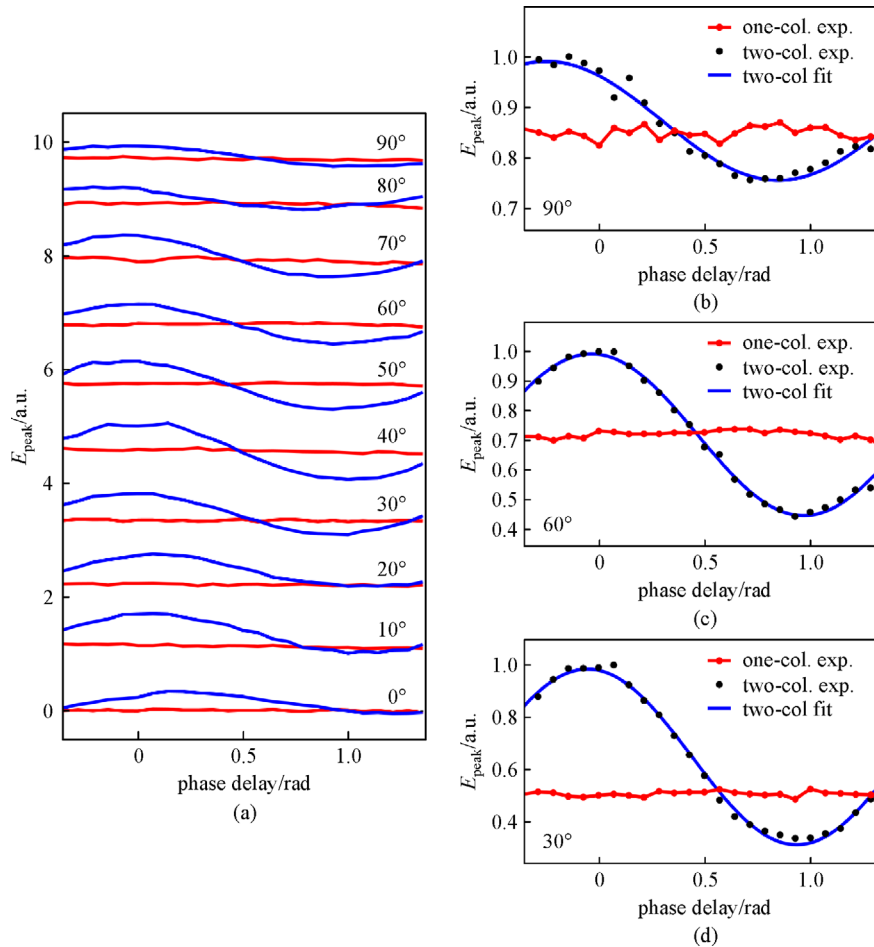
Fig. 23   (a) THz peak amplitude as a function of the relative phase between FB and SH for the one-color (red) and two-color (blue) cases for different detection angles. The curves are offset for clarity. (b), (c) and (d) shows more clearly the experimental data for angle of 90°, 60°, and 30° respectively. Dots are experimental data, while blue line is the fitting of the two-color data with a sine function

contribution (red curves). The latter are obtained by rotating α such that the SH harmonic is minimized. As expected, they do not show any dependence on the position of the crystal.

Finally, the spectra obtained in the one-color and two-color are plotted as function detection angle in Figs. 24(a) and 24(b). The spectral shape and the bandwidth are very similar on both cases, see also Fig. 24(c) for a clearer comparison. This is unlike what previously observed when comparing the spectra from one-color microplasma and two-color elongated plasma (Fig. 19(a)).

3.3   Generation mechanism

The radiation pattern from the microplasma source is significantly different from that of elongated plasmas. The main direction of radiation is, in fact, almost orthogonal to the laser propagation and spatially separated from the laser excitation beam. Conversely, for elongated plasmas, both in the one-color and two-color approaches, despite very different generation mechanisms, it was shown that THz is emitted as a forward propagating cone whose divergence

angle increases as the length of the plasma string decreases [95,108,111].

The experimental findings in condition of high NA focusing are all consistent with the interpretation of THz emission from "one-color" plasma given by Hamster and coworkers [88,93]. Coherent THz radiation originates from plasma currents driven by the laser ponderomotive force. This force is proportional to the local intensity gradient and therefore it is not strongly affected by polarization rotations of the linearly polarized laser field (Figs. 13 and 14). The measured radiation pattern in Fig. 9(a), whose peak is almost orthogonal to the laser propagation direction, suggests that THz radiation originates from longitudinal plasma currents.

To understand the origin of this current, let us focus on the effects of the ponderomotive force on the charged particles forming the plasma. In presence of an inhomogeneous electric field, charged particles experiencing this force are pushed toward region of lower field intensity. This is depicted for the case of a focused laser beam in Fig. 25.

As soon as the front of the optical excitation pulse
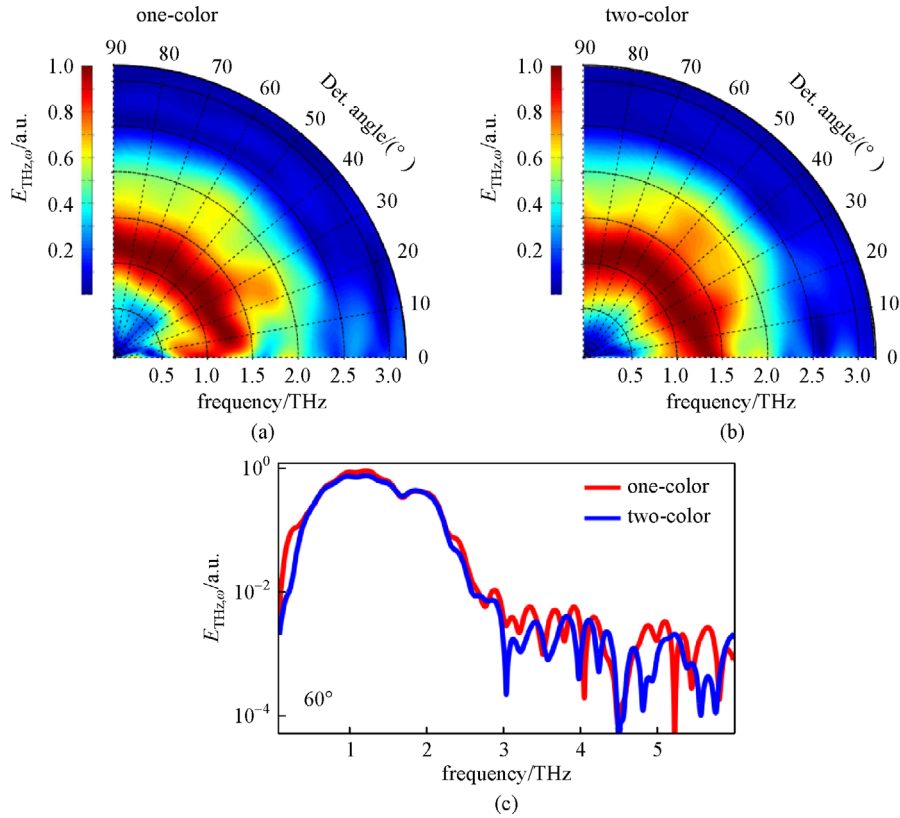
Fig. 24 Density plot representing the angle-dependent spectral emission from a microplasma generated with the reflective objective and laser pulse energy of 90 μJ. The plot is obtained through spline interpolation of the Fourier transform of ten THz waveforms recorded at different detection angles in 10° intervals starting from 0° obtained in the one-color (a) and two-color (b) cases. (c) Spectral amplitude measured at a detection angle of 60° in the one-color (red) and two-color (blue) cases. All the spectra are normalized to one to show how the spectrum does not change appreciably with detection angle. However, by doing so the reader could be lead to believe that there is a strong emission for detection angle close to 0°. This is not the case as the amplitude of the spectra measured at 0° and 10° are more than one order of magnitude lower than those measured at larger angles
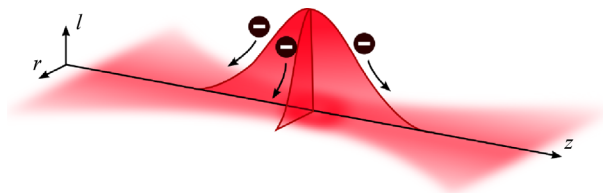

Fig. 25 Visual representation of the action of the ponderomotive force. The picture shows in red the intensity profile of a focused laser beam along the propagation axis and any radial direction. Charged particles close to the focal volume are pushed toward region of lower intensity

reaches the ionization threshold, electrons and ions are created (Fig. 26(a)). Initially charges are distributed homogeneously and there is no net charge density, defined as the difference between the electrons and ions distributions. Both type of particles experiences the ponderomotive force from the time of birth to when the laser pulse leaves the plasma volume. However, compared to electrons, the ions are many orders of magnitude heavier

and can be considered at rest for the ultrafast time scale of the laser pulse, hence we can focus our attention just on the motion of the electrons. Those are locally accelerated toward area of lower intensity. Over the time duration of the laser pulse, many electrons are pushed backward, effectively creating a dipole along the laser propagation direction moving at the group velocity of the femtosecond excitation pulses (Fig. 26(b)). Electrons are not pushed forward as the intensities considered in our experiments are not relativistic, i.e., the electrons travel at speed much lower than that of the optical pulse. The electrons that are pushed in the radial directions exit the interaction volume between the laser and the plasma at timescales of the optical field oscillation (~2.7 fs at 800 nm), which are too short to result in contributions to the THz emission. Finally, after the laser pulse exits the plasma, the restoring force between the spatially separated charges brings them close again (Fig. 26(c)).

Therefore, the action of the ponderomotive force is to induce a transient space charge separation in the vicinity of the focal plane [88,93] creating a longitudinal plasma current oscillation. This can be thought as a traveling
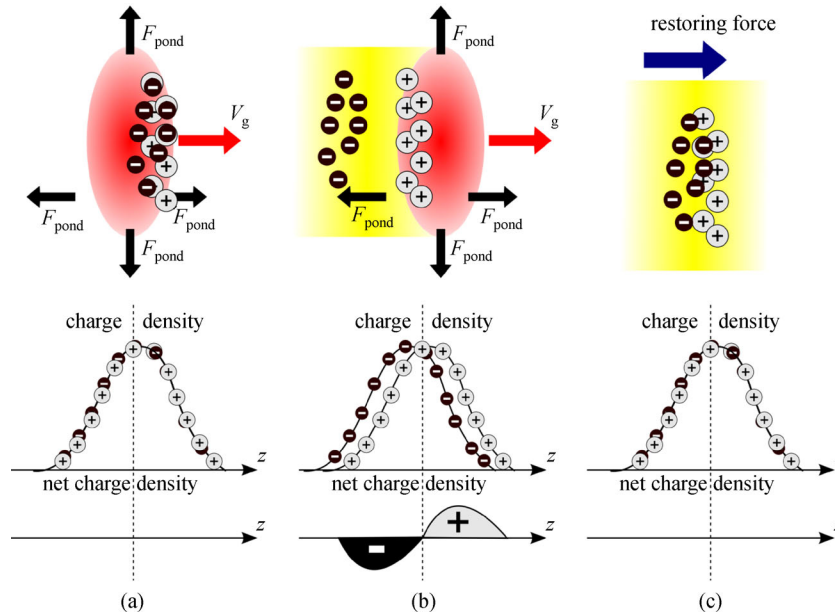
Fig. 26 Longitudinal currents from which THz radiation originates is formed in a three steps process. (a) Electrons and ions are created at the front of the laser pulse; (b) Ions can be considered still due to their mass, while electrons are pushed backward from them by the ponderomotive force. The spatial separation between ions and electrons creates a net charge density behind the ionization front which acts as an effective dipole; (c) After the laser pulse leaves the plasma the charges are brought back together by the restoring force due to Coulomb attraction

dipole behind the ionization front of the excitation laser, oscillating with a period close to the time duration of the optical pulse, hence radiating an electromagnetic transient with frequencies in the THz range. The surge of this ultrafast longitudinal plasma current is the result of a time average effect depending only on the envelope of the optical pulse and not on the dynamics of single ionization events.

In the one-color approach, the following estimate scaling law for the THz peak power P_{THz} as a function of the relevant laser source parameters has been proposed by Hamster and coworkers [93]:

$$P_{THz} \propto \frac{(W \cdot NA \cdot \lambda)^2}{\tau^4}, \quad (4)$$

where W is the laser pulse energy, NA is the numerical aperture of the focusing laser cone, λ is the laser wavelength and τ is the pulse duration. This simple analysis does not rigorously take into account all of the phenomena that may affect the THz generation process and its validity has not been fully tested experimentally, however, it provides an interesting insight. In fact, it suggests that a tight focusing geometry with high NA optics allows both decreasing the laser energy threshold, by increasing the laser intensity at the focal plane, and improving the THz generation efficiency. Indeed, our experimental approach was to maximize the ponderomotive force by focusing the laser field with high NA optics, leading to estimated peak intensities at the focal point

exceeding 10^{15} W/cm^2 and a very steep intensity gradient around the focal volume.

The gathered experimental evidence supports some of the finding of Eq. (4): 1) The THz peak power is indeed a quadratic function of the laser pulse energy, see Fig. 15; 2) while the THz peak power increases with the NA of the focusing lens, the dependence found was less than quadratic (see Fig. 16 and Table 3); 3) finally, in my experience the optical to THz efficiencies were higher using the longer laser pulse duration, therefore strongly disagreeing with Eq. (4); 4) the wavelength dependence was not tested.

Remarkably, the 1D analytical model proposed to explain the forward THz emission from filaments within the framework of transition-Cherenkov-like emission described in Ref. [134] would also qualitatively describe the radiation pattern when the length of the filament is reduced to 40 μm, as shown in Fig. 9.

The THz emission is calculated as the far-field radiation of a longitudinal plasma current $j_z(\omega)$. The energy spectral density emitted in the unit solid angle is [134]

$$\frac{d^2 W_{THz}}{d\omega d\Omega} \propto |j_z(\omega)|^2 f(\omega, \theta, L), \quad (5)$$

$$f(\omega, \theta, L) = \frac{\sin^2\theta}{(1-\cos\theta)^2} \sin^2\left(\frac{L\omega}{2c}(1-\cos\theta)\right), \quad (6)$$

where θ is the emission angle, L is the longitudinal length of the plasma column, and c is the speed of light.

Figure 27 shows, as example, the predicted radiation pattern for a frequency of 1.5 THz for three different plasma lengths. The THz emission is oriented in the forward direction for longer plasma lengths and move away from the laser optical axis as the plasma size is reduced. Comparing to elongated plasma, the shorter the plasma length the wider is the THz radiation pattern.

To compare the model to our experimental results, for each value of detection angle Eq. (5) was numerically integrated over the frequency interval accessible with our detection technique (0.1 to 2.5 THz) and over the detection solid angle. For our experimental conditions we estimated the electron densities to be greater than 10^{18} cm^{-3}, corresponding to plasma frequencies higher than 9 THz, and electron collision frequencies much smaller than the plasma frequency. As shown in Fig. 28, this simple analysis correctly predicts the angle of maximum emission and qualitatively agree well with all the experimental data.

The radiation pattern is mainly described by the geometrical factor $f(\omega,\theta,L)$, which describes the far-field summation of radiation coming from a source moving at the speed of light over a finite length L, and it is loosely affected by the spectral content of the excitation current $j_z(\omega)$.

3.4   Section summary

In this section, the use of microplasmas as a broadband THz wave source was demonstrated. The authors mea-sured THz waveforms generated with laser pulse energies as low as 660 nJ, which is an improvement close to two orders of magnitude compared to the state of art.

The radiation can be visualized as a forward propagating cone with a very high divergence angle. The THz emission is locally linearly polarized, and oscillating in the plane defined by the laser excitation propagation axis and the local THz propagation axis.

The emission from the microplasma can be intuitively visualized as the emission from a dipole antenna, which is characterized by the presence of two lobes oriented orthogonally to its axis. In the microplasma, however, the current is not fed externally, but it is due to an effective dipole created behind the ionization front of the laser excitation. This dipole-like source moves at the group velocity of the optical pulse over a finite length, causing the lobes not to be exactly orthogonal to the laser propagation direction. The radiation pattern can be explained within the framework of transition-Cherenkov-like emission, which remarkably provides a qualitative description of the THz radiation from "one color" plasmas over more than seven order of magnitude differences in plasma length, from tenths of micron to tenths of centimeter.

The coherent nature of the emission suggests that more complicated, even arbitrary, radiation patterns might be achieved by combining the radiation from multiple microplasmas, similarly to a phase array. Moreover, the combination of a radiation pattern where the THz emission is spatially separated from the laser excitation and of a sub-wavelength source size (1 THz = 300 μm) might promote
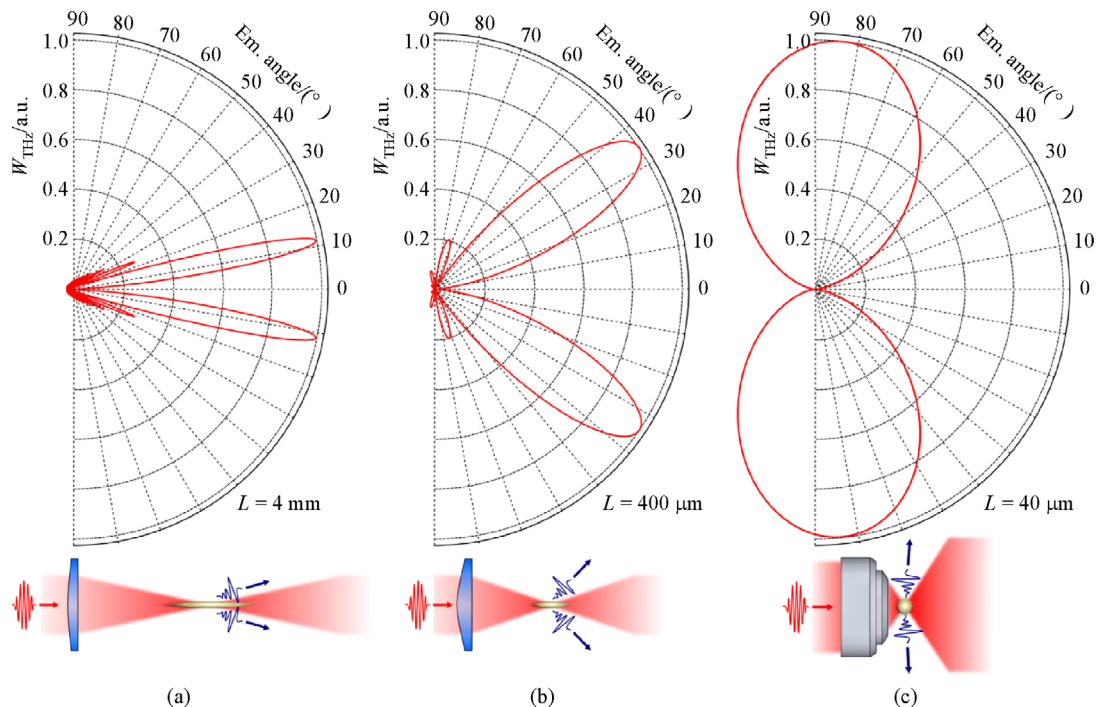
Fig. 27   Theoretical radiation pattern at a frequency of 1.5 THz of plasmas of lengths (a) 4 mm, (b) 400 μm and (c) 40 μm
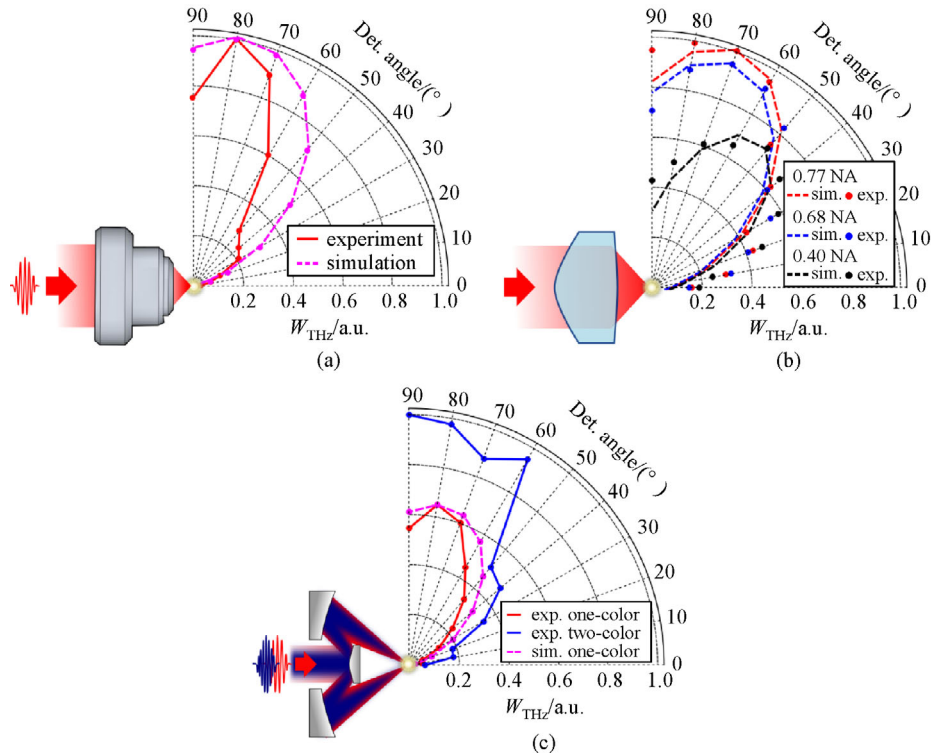
Fig. 28 Comparison of the radiation patterns calculated with numerical simulation and those measured experimentally. (a) one-color scheme, 40 μm plasma length: experiment (red solid), simulation (dashed, magenta); (b) one-color scheme, 72 μm plasma length (0.77 NA lens), red (simulation, dashed line, experiment, dots); 78 μm plasma length (0.68 NA lens), blue (simulation, dashed line, experiment, dots); 120 μm plasma length (0.40 NA lens), black (simulation, dashed line, experiment, dots); (c) two-color scheme, 40 μm plasma length (0.45 NA Schwarzschild reflective objective): one-color experiment (red, solid); one-color simulation (magenta, dashed); two-color experiment (blue, solid)

new applications, such as plasma-based THz near-field techniques.

Further optimization of the technique, including improved design of the THz collection optics, the use of longer excitation laser wavelengths has the promise to untap the full potential of plasma-based THz techniques with low energy ultrafast lasers.

4 Detection of terahertz radiation with microplasma

The use of ambient air laser-induced microplasmas as THz sensors is demonstrated. This is accomplished by implementing the THz-REEF detection scheme in counter-propagation geometry. This particular arrangement was not explored even in the case of elongated plasma.

4.1 Counter-propagation THz-REEF with elongated plasmas

The THz-REEF detection method has been introduced in Section 2.3. In this technique, a laser plasma is employed as a "sensor" by measuring the fluorescence emission

enhancement induced by the presence of the THz radiation. With elongated plasmas THz-REEF detection has been implemented by having the THz and optical pulses propagate with the same direction, i.e., their propagation vectors are parallel and pointing in the same direction.

However, for the microplasma case, in order to accommodate the short working distance of the focusing optics, the THz-REEF technique needs to be implemented in a counter-propagating fashion in which the THz and the optical pulses propagate in opposite directions. Both schemes, respectively referred to as "copropagation" and "counter-propagation" geometries, are depicted in Fig. 29 (a). As the latter configuration has never been explored, it was initially demonstrated with elongated plasma.

The experimental setup is similar to that employed by Liu and Zhang in Ref. [91], to which the reader is referred for more details. The setup implements the standard time-domain interferometer as described in Section 2.1. The laser employed was Spectra Physics Hurricane (800 nm, 100 fs, 0.8 mJ, 1 kHz). Strong single cycle THz pulses with peak field of 90 kV/cm were obtained via optical rectification in $LiNbO_3$ with titled pulse front geometry [56]. The THz radiation was collected and refocused on the
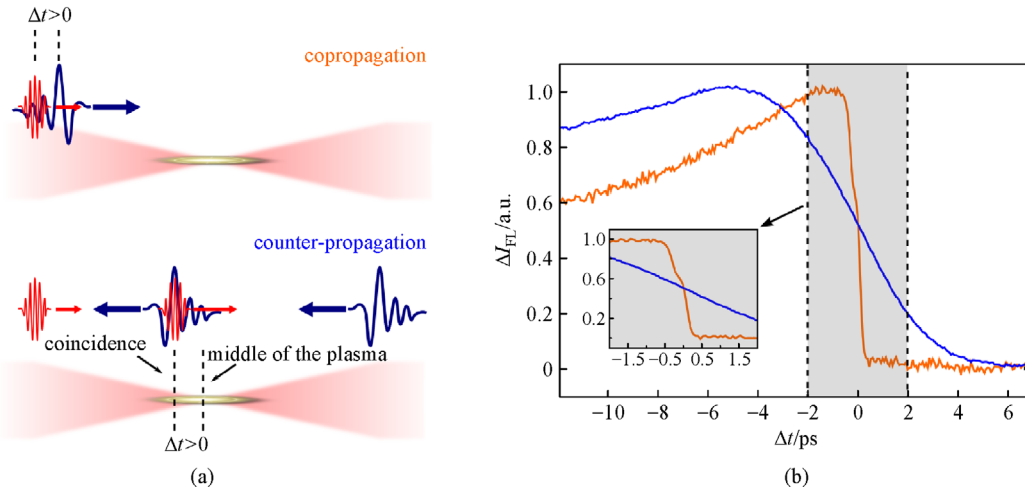
Fig. 29 (a) Interaction geometries. Top: in copropagation geometry the THz (blue) and optical (red) pulses travel in the same direction. Δt is the time delay between the two. Bottom: in counter-propagation geometry the THz and pulses travel in opposite direction. In this case Δt defines the position along the optical propagation axis at which the THz and optical pulses meet. (b) Plasma fluorescence intensity enhancement as a function of Δt in copropagation (orange) and counter-propagation (blue) geometries. Both curves are normalized to one

plasma formed by focusing the probe beam. The plasma fluorescence is imaged into the input slit of a grating monochromator and measured with a PMT placed at its output slit. The setup could be easily switched through flip mirrors between the copropagation and counter-propagation geometries. The plasma was generated by focusing 150 µJ laser energy with a plano-convex lens having an EFL of 4 inches resulting in a plasma length of ∼ 630 µm. The REEF trace is obtained by measuring the fluorescence emission line centered at 337 nm as a function of the time delay, Δt, between the THz and the probe pulses. The interpretation of the time delay is different for the two schemes. In the copropagation one, as both pulses travel in the same direction, Δt is the time delay between their peaks. Positive values are defined such that the THz pulse leads the optical pulse. In the counter-propagation case, Δt defines the position along the optical axis at which the THz and optical pulses meet. Δt equals to zero corresponds to the condition in which the pulses meet at the center of what would be the final plasma extension. For positive values, the THz pulse arrives at the plasma midline earlier than the optical pulse, and therefore they meet each other toward the beginning of the plasma. The definition of Δt is presented graphically in Fig. 29(a).

The comparison between the REEF traces obtained in both configurations is shown in Fig. 29(b). Those traces depict the fluorescence absolute enhancement, ΔI_{FL}, obtained by subtracting the background fluorescence, i.e., fluorescence intensity in absence of THz radiation, to the signal measured with PMT. In both cases, the fluorescence signal starts increasing when the THz pulse begins to overlap temporally with the optical pulse at the plasma location. The copropagation trace (orange) shows a rapid increase of fluorescence comparable to the THz pulse time

duration, while the counter-propagation one exhibits a gentle rising slope close to 10 ps. Moreover, the slope of the copropagation trace shows a distinctive feature, shown in the inset of Fig. 29(b), whereas the one of the counter-propagation trace is smooth and featureless. The presence of this feature allows to retrieve the time-dependent THz intensity profile as previously demonstrated by Liu and Zhang [91], and will be discussed in more details in next section.

The fluorescence enhancement magnitude in both configurations is similar. Figure 30 depicts the fluorescence spectrum, showing the 2^+ system of N_2, in the cases of no THz illumination (black) and THz irradiation
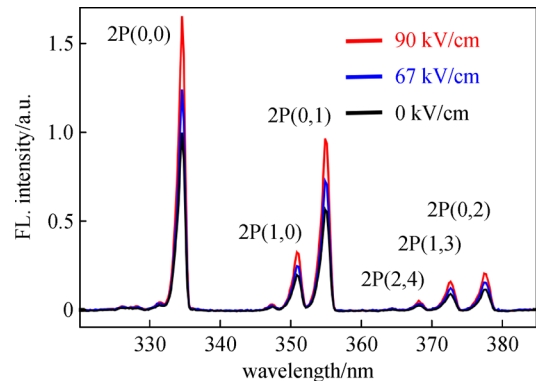
Fig. 30 Fluorescence intensity spectrum when no THz is applied (black) and for peak THz fields of 67 kV/cm (blue) and 90 kV/cm (red). The THz illuminates the plasma in counter-propagation geometry. All the emission lines belong to N_2 2^+ system. The numbers in parenthesis are the upper-lower vibrational levels of the transitions

in counter-propagation geometry with peak fields of 67 kV/cm (blue) and 90 kV/cm (red). With the highest THz peak field, a fluorescence enhancements exceeding 60% were achieved.

The interaction of the THz pulse and the plasma in the counter-propagation geometry was further studied by combining the temporal information retrieved using the time-domain interferometer with spatial information obtained with a gated iCCD camera (Princeton Instruments PIMAX 3) synchronized with the laser. The plasma was imaged from the side through a narrowband filter centered at 337 nm, so to reject scattered light from the laser (Fig. 31 (a)). The gate time was chosen to be 3 ns, the shortest possible available with our instrument. The images were calibrated using a 100 μm pinhole as target.

Images of the plasma were recorded with and without THz illumination for different values of time delay Δt between the THz and optical pulses. Those values were chosen using the REEF trace measured with the PMT so to cover the whole slope of the raising fluorescence intensity.

For each value of Δt, it was possible to obtain the spatially resolved fluorescence enhancement by subtracting the image taken when the THz pulse illuminates the plasma from the one when it is not. The plasma profiles with and without THz illumination and the retrieved fluorescence enhancement corresponding to the peak of the REEF trace ($\Delta t = -7.3$ ps) are plotted in Fig. 31(b) as solid blue, dashed blue and red lines respectively. This picture shows that the fluorescence intensity is not increased over the whole plasma length but only for values of z less than roughly 300 μm. This distance value corresponds to the point in space where the THz pulse meets the ionization front of the optical pulse for the specific value of Δt at which the image is taken. For values of z higher than 300 μm, the plasma is formed after the passage of the THz pulse and therefore its fluorescence cannot be enhanced by it. For different values of Δt, the THz pulse and the ionization front meet at different locations respect to the plasma midpoint, spatially moving the onset of fluorescence enhancement as clearly demonstrated in Fig. 31(c). For high (low) enough values of Δt, the THz and optical pulses meet outside the region of high intensity where the
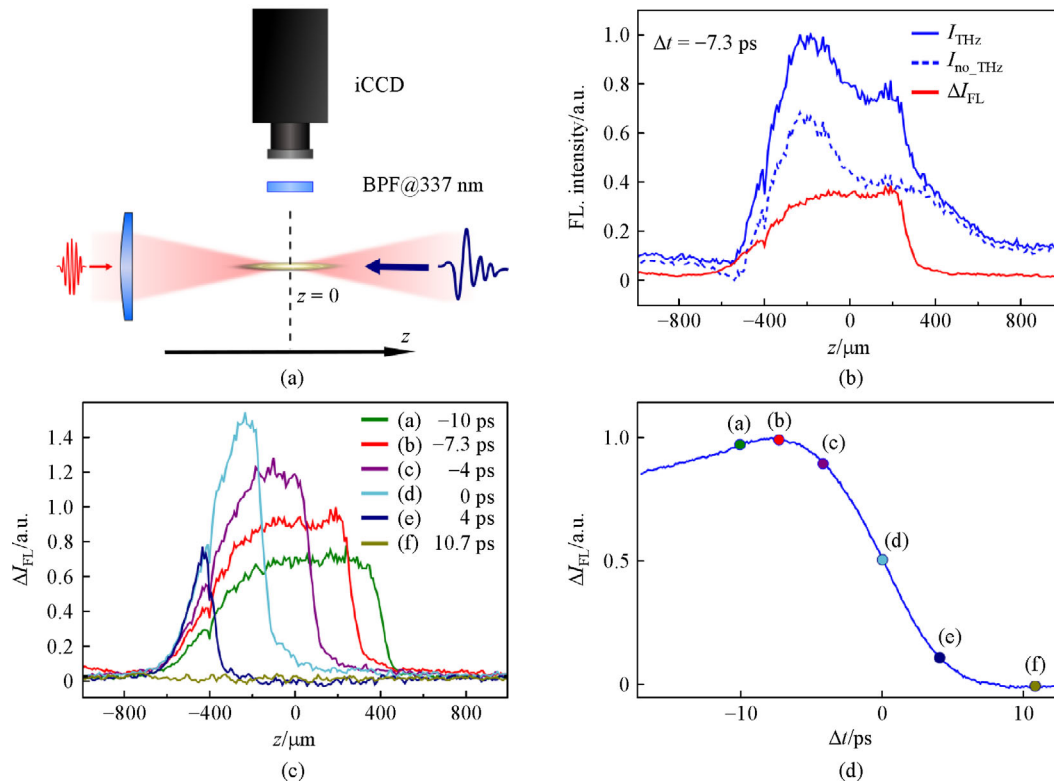
Fig. 31 (a) Experimental setup. The optical (red) and THz (blue) pulses travel in opposite direction. The plasma is imaged from the side with an iCCD camera through a narrowband filter centered at 337 nm. (b) Plasma fluorescence cross-sections with (blue) and without (dashed blue) THz illumination. The red curve is the spatially resolved fluorescence enhancement calculated by subtracting the fluorescence profile with and without THz illumination. (c) Spatially resolved fluorescence enhancement traces for different values of Δt. As Δt increases, the onset of the enhancement moves along the plasma toward the direction which the optical pulse comes from. (d) Plasma fluorescence intensity enhancement as a function of Δt in counter-propagation (blue) geometry. The colored points represent the area underneath the curves of (c) of the corresponding color and letter

plasma can be created and no fluorescence enhancement occurs.

The area underneath each curve in Fig. 31(c) is equivalent to a single point in the time-dependent REEF trace. In fact, the superposition of the points calculated as the integral of the various spatially-resolved fluorescence enhancement curves with the time-dependent REEF trace measured with the PMT matches perfectly, see Fig. 31(d).

4.2   Counter-propagation THz-REEF with microplasmas

By changing the focal length of the focusing optics, it was possible to shorten the dimension of the plasma creating a microplasma. For this experiment, they were employed a 2 inches EFL and 1 inch EFL plano convex lenses and a 0.14 NA microscope objective obtaining microplasmas of length 100, 45 and 40 μm respectively.

The time-resolved REEF traces obtained with those focusing elements are plotted in Fig. 32. Each trace obtained in counter-propagation geometry is compared with the trace obtained in copropagation geometry with elongated plasma (orange). As opposed to the trace obtained with the 4 inches EFL lens discussed in the previous section, the ones obtained with microplasmas shows a steeper increase in fluorescence enhancement, and more importantly the slope is not featureless, but resembles a stretched version of the one encountered for the copropagation geometry. Hence, the REEF traces in counter-propagation geometry with microplasmas might encode information regarding the THz waveform, e.g., intensity or field time evolution or the plasma dynamics.

It is interesting to compare the fluorescence spectra and the REEF traces in the cases of tightest focusing, that is with 1 inch EFL lens, corresponding to 0.11 NA considering a beam size for our laser of 6 mm, and the 0.14 NA microscope objective. The fluorescence spectra with and without THz illumination are shown as a function of laser energy in Figs. 33(a) and 33(b) for the lens and the objective respectively. At low levels of laser energy the broadband continuum contributes little to the fluorescence emission. However, as the laser energy increases, it becomes significant and more so in the case of the microscope objective signaling the presence of higher laser intensities. As mentioned in the previous paragraph, the fluorescence enhancement due to THz radiation occurs only at the molecular lines and not over the continuum.

The REEF traces obtained with the lens (Fig. 33(c)) have a better SNR compared to those obtained with the objective. To offer a quantitative comparison between traces the author defined a REEF quality factor as a metric. This was found to be necessary as the quality of the REEF traces are affected by many parameters, such as the laser energy, the laser chirp, the gain setting of the PMT and of its current amplifier. The desired qualities of a REEF trace are: 1) highest fluorescence enhancement relative to the
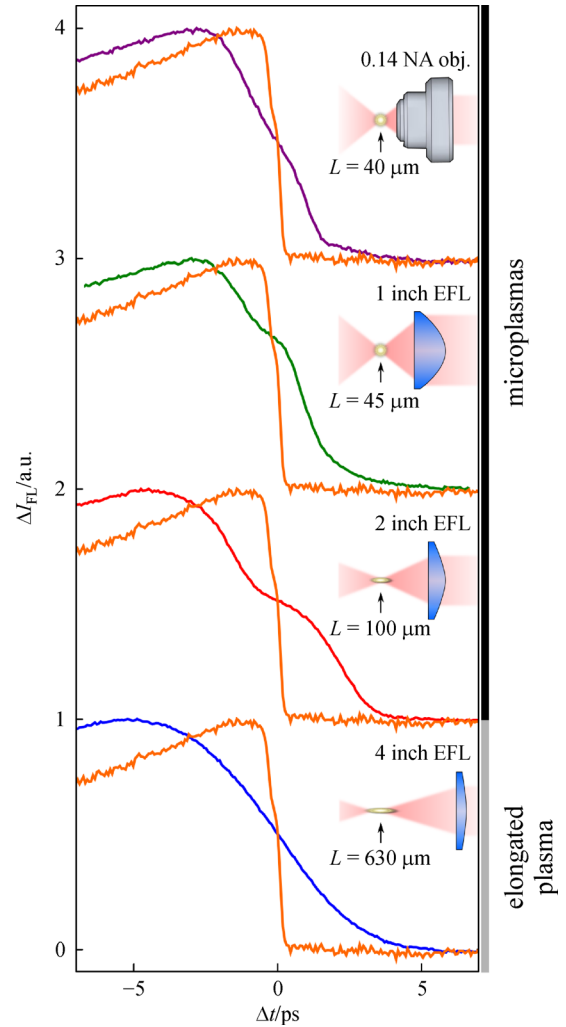
Fig. 32 Plasma fluorescence intensity enhancement as a function of Δt from plasmas obtained with the following optic components: 4 inch EFL plano-convex lens (blue); 2 inch EFL plano-convex lens (red); 1 inch EFL plano-convex lens (green); 0.14 NA microscope objective (purple). The plots are offset for clarity. Each trace in counter-propagation geometry is plotted together with the one in copropagation geometry obtained with the 4 inch EFL plano-convex lens (orange). Each curve is normalized to one

background and 2) highest SNR of the fluorescence signal. Therefore, the figure of merit was defined as the product of the two:

$$\mathrm{FM_{REEF}} = \Delta I_{\mathrm{FL,rel}} \cdot \mathrm{SNR}$$

$$= \frac{\langle \mathrm{Peak_{FL}} \rangle - \langle \mathrm{Bg_{FL}} \rangle}{\langle \mathrm{Bg_{FL}} \rangle} \cdot \frac{\langle \mathrm{Bg_{FL}} \rangle}{\mathrm{std}(\mathrm{Bg_{FL}})}$$

$$= \frac{\langle \mathrm{Peak_{FL}} \rangle - \langle \mathrm{Bg_{FL}} \rangle}{\mathrm{std} \langle \mathrm{Bg_{FL}} \rangle}, \tag{7}$$

where $\langle \mathrm{Peak_{FL}} \rangle$ is the mean value of the peak fluorescence in the REEF traces, $\langle \mathrm{Bg_{FL}} \rangle$ is the mean value of the
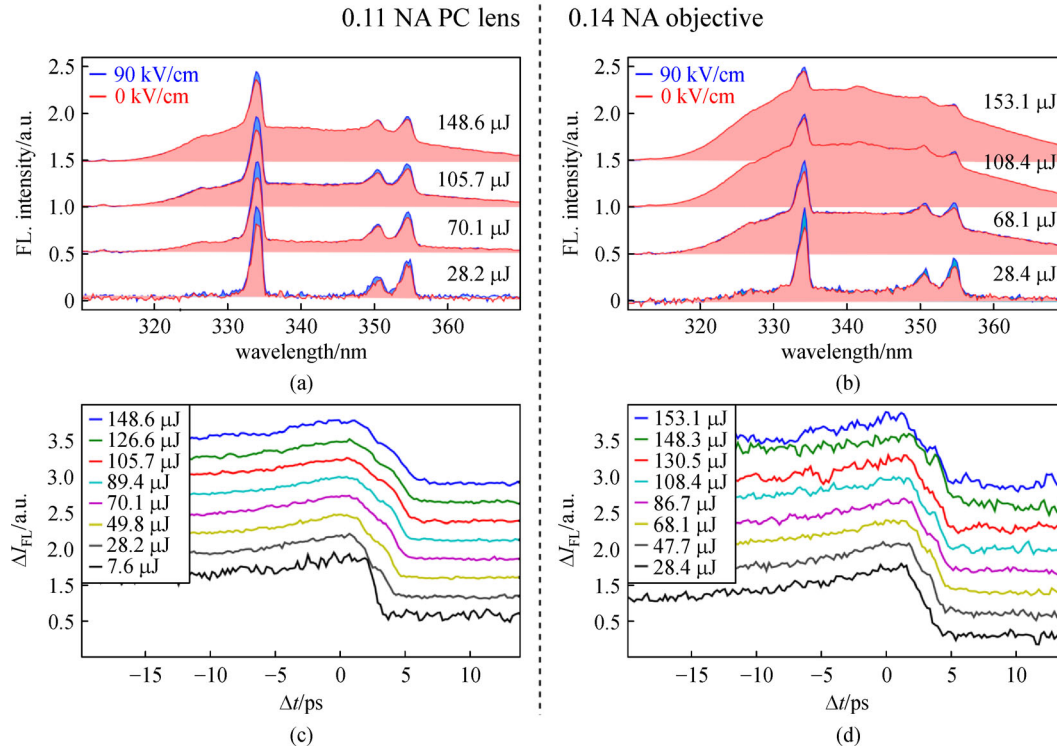
Fig. 33   (a) and (b) Fluorescence intensity spectrum when no THz is applied (red) and peak THz field of 90 kV/cm (blue) for different values of laser energy. The microplasmas are obtained with (a) 1 inch EFL plano-convex lens and (b) the 0.14 NA microscope objective. (c) and (d) Plasma fluorescence intensity enhancement as a function of Δt for different values of laser energy. All curves are normalized to one. The microplasmas are obtained with (c) 1 inch EFL plano-convex lens (d) the 0.14 NA microscope objective

background fluorescence, i.e., value of the REEF trace for high Δt, and std$\langle$Bg$_{FL}\rangle$ is the standard deviation of the background fluorescence.

The REEF traces obtained with the lens and the objective for different values of laser energy are compared using the relative enhancement, $\Delta I_{FL,rel}$, and the figure of merit FM$_{REEF}$. The relative enhancement measured at the emission 337 nm emission line increases as the laser energy decreases (Fig. 34(a)). This is attributed to two facts: 1) the highest the laser energy the highest is the number of ionized molecules, therefore the smaller is the

available number of electrons that can be further promoted to the free state by THz radiation; 2) the highest the laser energy the highest is the contribution to the background of the fluorescence continuum, which is not affected by the presence of THz radiation. Those two reasons explain also why the relative enhancement obtained with the lens are higher than those obtained with the microscope objective.

Interestingly the factor of merit shows that there are optimal laser energy levels that optimize the quality of the REEF trace (Fig. 34(b)). In fact, despite the relative enhancement increases as the laser energy decreases, the
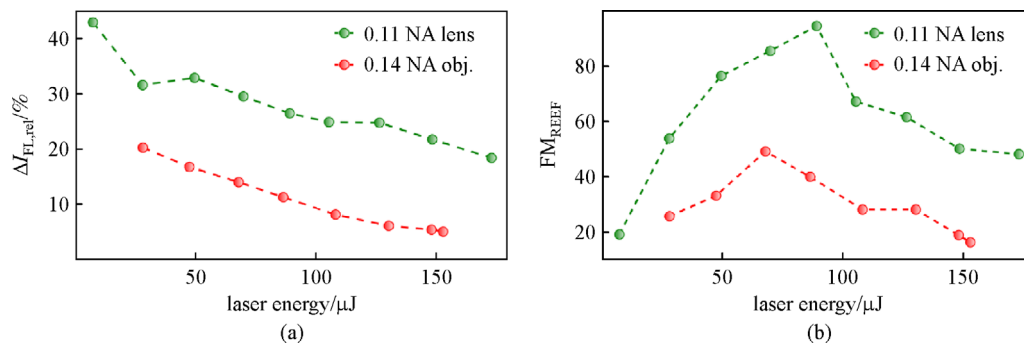
Fig. 34   (a) Relative fluorescence enhancement as a function of laser energy for microplasmas obtained with 1 inch EFL plano-convex lens (red) and 0.14 NA microscope objective (green). (b) REEF figure of merit as a function of laser energy for microplasmas obtained with 1 inch EFL plano-convex lens (red) and 0.14 NA microscope objective (green)

SNR decreases due to the lower value of fluorescence intensity. For the lens the best compromise was found for laser energies around 90 μJ, whereas for the objective it was around 70 μJ. Also the quality of the REEF traces obtained with the 1 inch lens was significantly higher than those obtained with the 0.14 NA objective.

Finally, the figure of merit was used to compare the quality of REEF traces obtained in all the configurations studied. The results are summarized in Table 4.

Except for the case of the 0.14 NA objective, the quality of the traces obtained in counter-propagating geometry with both elongated plasma and microplasma is equivalent, if not better, compared to the one of the trace obtained in copropagation geometry with elongated plasma.

4.3 Toward coherent detection with microplasmas: future work and open questions

A microplasma is capable to sense the presence of THz radiation through REEF. In principle this is also possible in copropagation geometry, however its realization is not practical, unless the laser microplasma can be generated with working distances greater than several inches. The measured trace contains information regarding the time-dependent THz intensity and the plasma dynamics. However, in order to retrieve them, the mechanism that encodes the THz intensity evolution into the fluorescence trace needs to be fully understood. Currently this is still an open question, which can be interpreted as an opportunity to improve our understanding of the REEF process and might open new applications for this technique.

To understand where the problem arises, let us start with the description of the REEF process in copropagation geometry, which has been described by Liu and coauthors in several manuscripts [91,116,118].

In the case of plasma created by the fundamental beam in a high pressure gas, which applies to ambient air, the plasma fluorescence enhancement ΔI_{FL} can be expressed by the following expression [91]:

$$\lim_{\tau \ll \tau_{\mathrm{THz}}} \Delta I_{\mathrm{FL}}(\Delta t) \propto n_{\mathrm{e}}\Delta t \int_{\Delta t+t_{\varphi}}^{+\infty} E_{\mathrm{THz}}^{2}(t)\mathrm{d}t, \qquad (8)$$

where n_{e} is the electron density, t_{φ} is a phase delay caused by the plasma formation dynamics at the early stage. In this limit, ΔI_{FL} is proportional to the THz energy and the instantaneous electron density.

This model well describes typical REEF curves in copropagation geometry that we routinely measure in the laboratory. The derivative of ΔI_{FL} is proportional to the

time-dependent THz intensity as shown in Fig. 35.

In copropagation geometry, as the optical and THz pulses travel in the same direction, the length of the plasma does not influence the shape of the REEF trace, but can only influence its amplitude. Conversely, in counter-propagation geometry the REEF trace heavily depends on the plasma length. As we have already observed in Fig. 32, when the plasma length decreases the slope of the trace becomes steeper, and, for short enough plasmas features appear in the traces.

The space dependencies can be included in Eq. (8) so that this model could be compared to the results obtained in counter-propagation geometry. The resulting expression is

$$\lim_{\tau \ll \tau_{\mathrm{THz}}} \Delta I_{\mathrm{FL}}(\Delta t)$$

$$\propto \int\int_{-\infty}^{+\infty} \mathrm{d}t\mathrm{d}z n_{\mathrm{e}}\left(z,t-\Delta t\overline{+}\frac{z}{c}\right) E_{\mathrm{THz}}^{2}\left(z,t-\frac{z}{c}\right). \qquad (9)$$

By changing the sign in front of the propagation term $\frac{z}{c}$ inside of $n_{\mathrm{e}}\left(z,t-\Delta t\overline{+}\frac{z}{c}\right)$ the equation describes the cases of copropagation (minus sign) and counter-propagation (plus sign). We note that the equation does not describe the interaction of the THz beam and the plasma when the directions of propagation are arbitrary, including the case in which they are orthogonal (90°). The time dependence for n_{e} is discussed in Ref. [91], while for the space dependence the profile measured with the iCCD camera-was employed.

In counter-propagation geometry, this model closely describes the experimental data in the case of elongated plasma (Fig. 36(a)), but significantly fail to produce the features of the traces obtained with microplasmas (see Figs. 36(b), 36(c) and 36(d)). In particular, for shorter plasmas the model predicts a much-exaggerated slope for the REEF curve and also fails to reproduce the features within the slope.

In analogy to the copropagation case, one may compare the derivative of the REEF trace obtained in counter-propagation with the square of the THz waveform measured with electro-optic sampling. As an example, this is done using the data measured for the 2 inch EFL case. The derivative of the experimental data presents high level of noise (Fig. 37(a), dashed red line), however numerical processing can be employed to filter most of it. This is obtained by undersampling the experimental data and interpolating it with a cubic spline function. The derivative of the interpolated function, shown as solid

Table 4   Comparison of the REEF traces obtained in copropagation and counter-propagation geometry through the REEF figure of merit (FOM)

focusing element	copropagation	counter-propagation			
	4 inches EFL PC lens	4 inches EFL PC lens	2 inches EFL PC Lens	1 inch EFL PC Lens	0.14 NA objective
FOM	80.7	105.4	70.2	79.2	46.8
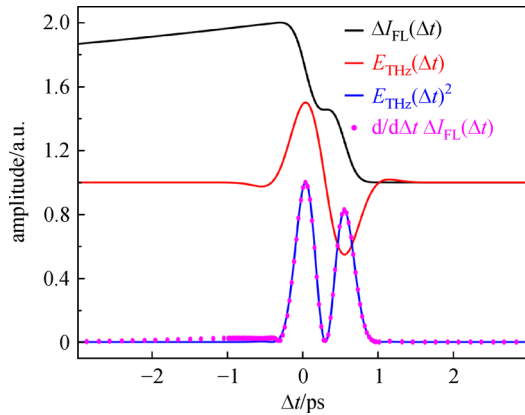
Fig. 35 Simulation of the REEF trace in copropagation geometry. The plot shows: the simulated plasma fluorescence intensity enhancement (black); the simulated THz waveform (red); the intensity as calculated by squaring the THz waveform (blue); the derivative of the plasma fluorescence intensity enhancement (fuchsia circles). The plasma fluorescence intensity enhancement curve and its derivative have been shifted of an amount $t_\varphi = 300$ fs so to show the overlap of the second with the THz intensity curve

black line in Fig. 37(a), is a filtered version of the derivative of the experimental data. The shape of the first one resembles the square of the THz waveform measured with electro-optic sampling but evolves at a longer time scale (Fig. 37(b)). While it is tempting to conclude that the counter-propagation REEF traces allow the retrieval of the time-resolved THz intensity, the author was not able to identify any physical mechanism that could produce a

time-stretched version of the THz intensity evolution as depicted in Fig. 37(b).

A more plausible interpretation of the counter-propagation REEF traces specifically addressing the presence of the "feature" inside the fluorescence raising slope and the unexpectedly slow rise time is suggested by computing the electron density spatial profiles that would produce the experimental curves presented in Fig. 32.

Those are obtained with a least-square fitting algorithm applied to Eq. (9) employing the experimental measured plasma profiles as the initial guess. The fitted curves and the respective computed plasma profiles are shown in Fig. 38.

Instead of representing the actual electron density spatial distribution, those curves are to be interpreted as the effective electron densities contributing to the REEF signals. Those curves suggest that the denser part of the plasma has very little contribution to the fluorescence enhancement, whereas the biggest contribution is due to the interaction of the THz wave with the outer region of the plasma, where the electron density is lower. This could be qualitatively explained by two physics phenomena: 1) the volumes with highest electron densities are the ones presenting the highest degree of ionization of the air molecules. It is therefore plausible that the contribution of those volumes to the THz-REEF signal is very small as the density of electronic states right below the continuum (~ 100 meV) is greatly reduced for highly ionized molecules. 2) For values of electron densities higher than 10^{16} cm^{-3}, which are achieved in the experiment being
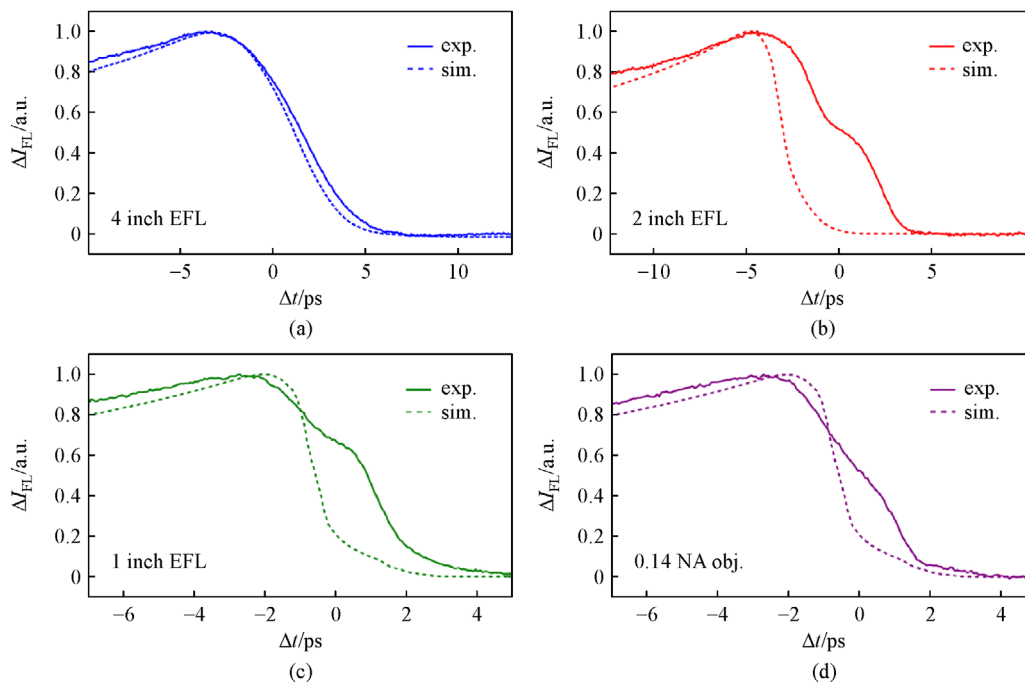
Fig. 36 Experimental (solid line) and simulated (dashed line) plasma fluorescence intensity enhancement as a function of Δt in counter-propagation geometry for the following focusing conditions (a) 4 inches EFL PC lens; (b) 2 inches EFL PC lens; (c) 1 inches EFL PC lens; (d) 0.14 NA microscope objective
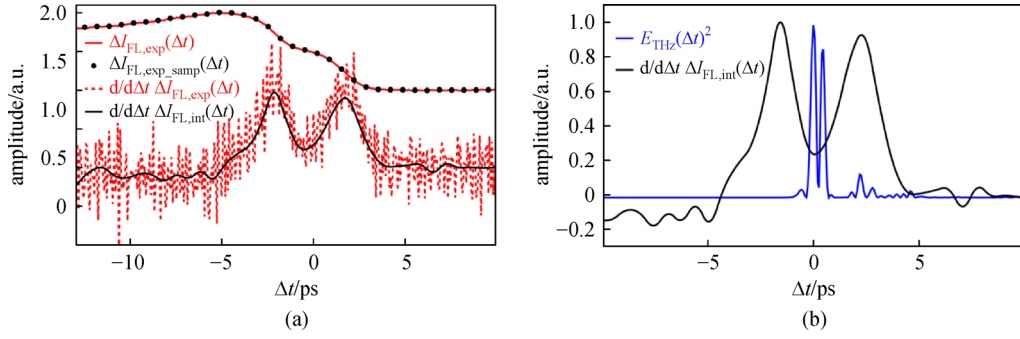
Fig. 37   (a) Experimental plasma fluorescence intensity enhancement as a function of Δt in counter-propagation geometry for 2 inches EFL lens case (solid red) and its derivative (dashed red). The black dots represented the sampling points of the experimental data used to construct an interpolated curve of the measured data. The derivative of the interpolated curve is shown as a solid black curve. The curves are offset for clarity. (b) The derivative of the interpolated curve (solid black) is compared to the square of the experimental THz waveform measured with electro-optic sampling (solid blue)
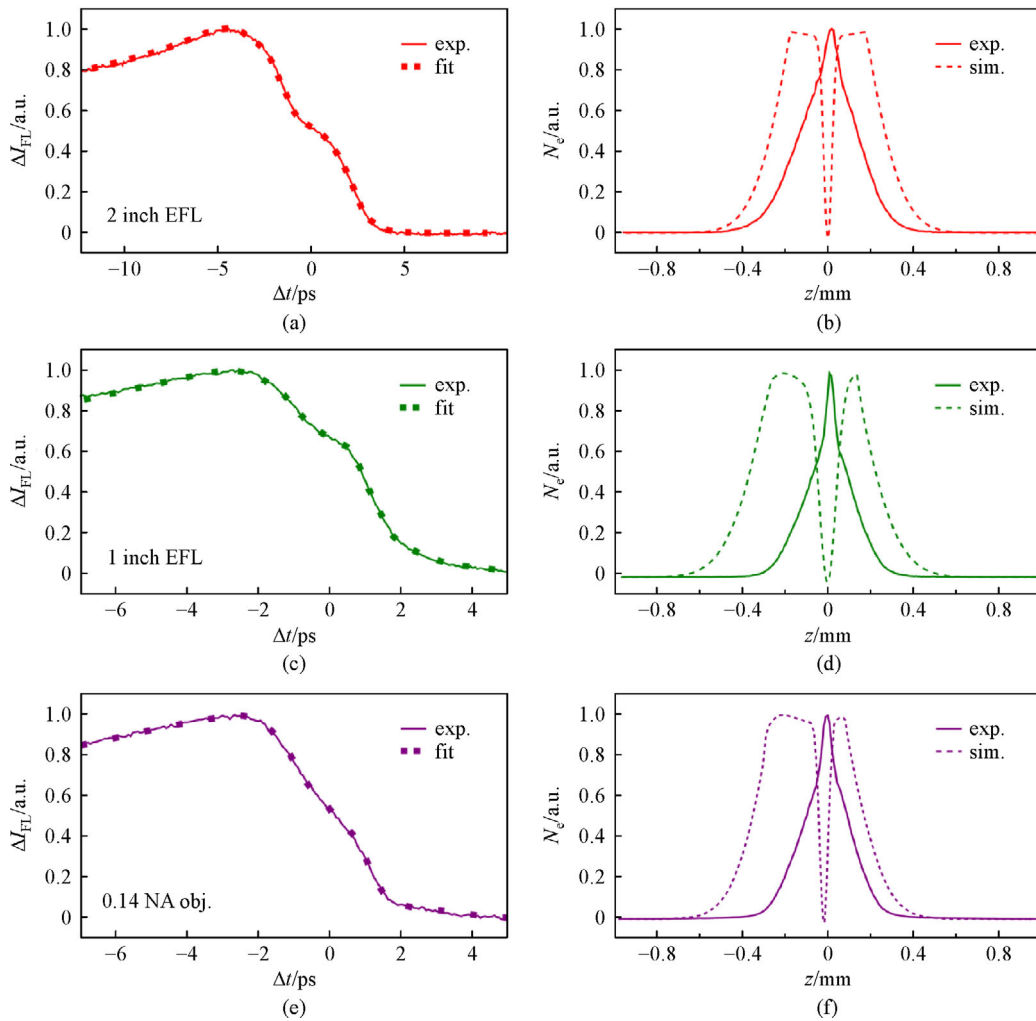
Fig. 38   Experimental (solid line) and numerical fitted (dashed line) plasma fluorescence intensity enhancement as a function of Δt in counter-propagation geometry for the following focusing conditions (a) 2 inches EFL PC lens; (c) 1 inches EFL PC lens; (e) 0.14 NA microscope objective. The respective electron densities are plotted in (b), (d) and (f). The solid lines represent the integration of the plasma fluorescence intensity along the radial dimension as measured with the iCCD camera, whereas the dashed line are the numerically evaluated plasma electron densities producing the curves plotted in (a), (c) and (e)

discussed, the plasma frequency becomes greater that 1 THz. Frequencies below that value are not allowed to propagate through the plasma, but they decay exponentially within a space defined by the skin depth of the plasma at the specified frequency. The skin depth gets smaller as the electron density increases. For the estimated electron densities of the experiment and the peak frequency of the input THz pulse (0.7 THz), the skin depth in the densest volume is as low as 5 μm. Therefore the densest part of the plasma is screened from the incoming THz pulse and do not contribute to the THz-REEF signal. It is the author belief that the interplay of both mechanisms produces the measured curves.

Those considerations suggest that the time-resolved intensity of the THz radiation might not be retrieved in the studied experimental conditions. A proposed experiment that could further explore this aspect is to use a dual-color laser beam to create the microplasma similarly to what has been demonstrated in copropagation mode [118]. One could study whether or not the measured REEF traces are affected by changing the relative phase between the fundamental beam and its second harmonic. The absence of a change would confirm that the features visible in the traces are just the result of the plasma density profile distribution and do not allow to retrieve the shape of the THz pulse.

The possibility of resolving the THz intensity evolution is however allowed by the theory for plasmas short enough to time-resolve field changes in the order of typical THz field oscillation times. A microplasma with a length of 15 μm would result in a time resolution of 50 fs, therefore allowing to accomplish this goal. As the THz-REEF process appears to require lower electron densities, the practical difficulty is that the fluorescence signal from such a short and low density plasma would be very small and close to the noise level of many optical detectors.

A more detailed study of the physical mechanisms producing the experimental curves might reveal the THz-REEF counter-propagation geometry as a useful tool for plasma diagnostics, potentially able to provide information regarding selected electronics states distributions not attainable with other techniques.

4.4   Section summary

The detection of THz pulses in counter-propagation geometry was demonstrated with both elongated plasmas and microplasmas through the REEF mechanism. The fluorescence enhancement and quality of the REEF traces, quantified through a figure of merit, is comparable to that obtained with elongated plasma in copropagation geometry.

The REEF traces in counter-propagation geometry for elongated plasma do not visibly contain any feature related to the time evolution of the measured THz pulse. In the case of microplasmas, however, the REEF trace shows distinctive features in the slope.

The theoretical model previously developed to explain the data measured in copropagation geometry describes well the experimental data in counter-propagation geometry only for the case of elongated plasma. However, for the microplasmas this model predicts much faster rising time for the fluorescence enhancement and also fails to reproduce the features measured experimentally.

That model assumes that the THz radiation interacts with the whole plasma volume independently of the plasma density and ionization degree of the molecules. This assumption is valid in the cases of elongated plasma studied in this dissertation for which the electron densities were low, less than 10^{15} cm^{-3}, however, it is not justified in the case of microplasmas were densities higher than 10^{18} cm^{-3} were reached. The computation of hypothetical effective electron density distributions that would reproduce the experimental data suggests that the densest volumes of the plasma do not contribute to the THz-REEF signal. Further experiments are necessary to confirm this hypothesis.

Currently the microplasma is able to "sense" the presence of THz radiation with performances close elongated plasmas in copropagation geometry, however the results presented herein suggest that the time-resolved THz intensity evolution might not be retrieved with this method. Nonetheless, THz-REEF in counter-propagation geometry could provide unique information for plasma diagnostics.

5   Conclusions

This review furthers the study of the particular field of THz science known as THz Air Photonics in which THz pulses are generated and detected using laser-induced plasmas in ambient air (or selected gases). Those techniques are very promising as they provide a platform for spectroscopy with broad spectral coverage, high peak electric fields, high spectral resolution and the possibility of remote operation.

In this draft, the authors studied the techniques of THz Air Photonics in the limit of very small plasmas, which were referred to with the name "microplasmas," as opposed to the usually employed plasmas, which were called "elongated plasmas."

The properties of the microplasmas as a source and sensor are qualitatively very different from those of elongated plasmas. Unlike many optical nonlinear generation phenomena, the coherent THz radiation is emitted with large divergence angles compared to the laser propagation direction, with the direction of maximum emission mainly dependent on the plasma length. The THz emission is locally linearly polarized, and oscillating in the plane defined by the laser excitation propagation axis and

the local THz propagation axis. The generation mechanism was attributed prevalently to space charge separation driven by the laser ponderomotive force and the radiation pattern explained within the framework of transition-Cherenkov-like emission, which remarkably provides a qualitative description of the THz radiation from "one color" plasmas over more than seven order of magnitude differences in plasma length, from tenths of micron to tenths of centimeter.

The microplasma emitter has been studied with "one-color" and "two-color" laser excitation. The second case more than doubles the optical-to-detected THz conversion efficiency maintaining similar radiation pattern.

The detection of THz pulses with a microplasma has been achieved through THz-REEF. The necessity of employing highly focusing optics having small working distances impeded the THz beam to propagate collinearly with the laser beam. Therefore the technique was implemented for the first time in counter-propagation geometry, in which the THz and laser pulses propagate in opposite direction. This geometry was first studied with elongated plasmas showing that the detection sensitivity is similar to the case in which the THz and laser pulses propagate collinearly, i.e., copropagation geometry. In the case of elongated plasmas the counter-propagation technique does not allow retrieving the temporal evolution of the THz pulse, unlike the copropagation geometry. However, when microplasma is employed distinctive features appears in the REEF trace. Those are tentatively explained as the result of the high plasma densities obtained in the microplasma case. In particular the experimental findings suggest that the densest volumes of the plasma do not contribute to the THz-REEF signal. For this reason, the implementation of microplasma as a sensor requires further study in order for it to be of significance for the field of THz science.

It is the authors opinion the counter-propagation THz-REEF geometry might reveal itself as a novel tool for plasma diagnostic in order to better understand the THz-plasma interaction and probe the dynamics of different electronic states in ionized molecules.

The implementation of THz Air Photonics techniques with microplasmas allowed the use of much lower laser pulse energies compared to those routinely used. In particular, the author measured THz waveforms generated with laser pulse energies as low as 660 nJ, which is the lowest reported laser pulse energy for THz generation in ambient air. Considering that the cost of the laser system is one of the big barriers against a more widespread use of THz Air Photonics, a significant reduction of the required laser energies might act as a catalyst for the diffusion of this promising approach. In fact, the use of oscillator lasers in THz air photonics has been hindered because they do not allow the generation of the typical elongated plasmas currently used. However, a simple estimation shows the feasibility for an oscillator to generate a microplasma.

Ambient air is ionized for laser peak intensity values of $10^{12} - 10^{13}$ W/cm². For our back of the envelope calculation, we can consider an ultrafast oscillator with the following parameters: 1 W average power, 10 fs pulse duration, 80 MHz repetition rate. The pulse energy for such laser source is 12.5 nJ, corresponding to a peak power of 1.2 MW, assuming a Gaussian profile. If we focus this source to a diameter of 1 μm, we are able to obtain a peak intensity of 10^{14} W/cm². For this value of intensity ambient air can be ionized and THz radiation will be emitted.

Other than the obvious advantage of the reduction of required laser energy, the microplasma offers some unique aspect compared to other THz sources and sensors. In fact the microplasma can be considered as a free-standing THz antenna with subwavelength size ($\sim\lambda/10$), with emission that is spatially separated from the laser excitation. Those characteristics might facilitate the coupling and interaction of THz radiation with microstructures and devices and promote new applications, such as plasma-based THz near-field techniques.

Moreover, the coherent nature of the emission suggests that more complicated, even arbitrary, radiation patterns might be achieved by combining the radiation from multiple microplasmas, similarly to a phase array.

Further optimization of the technique, including improved design of the THz collection optics, the use of longer excitation laser wavelengths, laser excitation transverse profile tailoring so to maximize the ponderomotive force, has the promise to express the full potential of plasma-based THz techniques with low energy ultrafast lasers.

References

1. Nuss M C, Auston D H, Capasso F. Direct subpicosecond measurement of carrier mobility of photoexcited electrons in gallium arsenide. Physical Review Letters, 1987, 58(22): 2355–2358

2. Exter M, Fattinger C, Grischkowsky D. Terahertz time-domain spectroscopy of water vapor. Optics Letters, 1989, 14(20): 1128–1130

3. Kolner B H, Buckles R A, Conklin P M, Scott R P. Plasma characterization with terahertz pulses. IEEE Journal of Selected Topics in Quantum Electronics, 2008, 14(2): 505–512

4. Jepsen P U, Cooke D G, Koch M. Terahertz spectroscopy and imaging- modern techniques and applications. Laser & Photonics Reviews, 2011, 5(1): 124–166

5. Ulbricht R, Hendry E, Shan J, Heinz T F, Bonn M. Carrier dynamics in semiconductors studied with time-resolved terahertz spectroscopy. Reviews of Modern Physics, 2011, 83(2): 543–586

6. McIntosh A I, Yang B, Goldup S M, Watkinson M, Donnan R S. Terahertz spectroscopy: a powerful new tool for the chemical sciences? Chemical Society Reviews, 2012, 41(6): 2072–2082

7. Kübler C, Ehrke H, Huber R, Lopez R, Halabica A, Haglund R F Jr, Leitenstorfer A. Coherent structural dynamics and electronic correlations during an ultrafast insulator-to-metal phase transition in VO2. Physical Review Letters, 2007, 99(11): 116401

8. Leahy-Hoppa M R, Fitch M J, Zheng X, Hayden L M, Osiander R. Wideband terahertz spectroscopy of explosives. Chemical Physics Letters, 2007, 434(4-6): 227–230

9. Davies A G, Burnett A D, Fan W, Linfield E H, Cunningham J E. Terahertz spectroscopy of explosives and drugs. Materials Today, 2008, 11(3): 18–26

10. Dai J, Xie X, Zhang X C. Detection of broadband terahertz waves with a laser-induced plasma in gases. Physical Review Letters, 2006, 97(10): 103903

11. Karpowicz N, Dai J, Lu X, Chen Y, Yamaguchi M, Zhao H, Zhang X C, Zhang L, Zhang C, Price-Gallagher M, Fletcher C, Mamer O, Lesimple A, Johnson K. Coherent heterodyne time-domain spectrometry covering the entire 'terahertz gap'. Applied Physics Letters, 2008, 92(1): 011131

12. Liu J, Zhang X C. Birefringence and absorption coefficients of alpha barium borate in terahertz range. Journal of Applied Physics, 2009, 106(2): 023107

13. Zalkovskij M, Zoffmann Bisgaard C, Novitsky A, Malureanu R, Savastru D, Popescu A, Uhd Jepsen P, Lavrinenko A V. Ultrabroadband terahertz spectroscopy of chalcogenide glasses. Applied Physics Letters, 2012, 100(3): 031901

14. D'Angelo F, Mics Z, Bonn M, Turchinovich D. Ultra-broadband THz time-domain spectroscopy of common polymers using THz air photonics. Optics Express, 2014, 22(10): 12475–12485

15. McLaughlin C V, Hayden L M, Polishak B, Huang S, Luo J, Kim T D, Jen A K Y. Wideband 15 THz response using organic electro-optic polymer emitter-sensor pairs at telecommunication wavelengths. Applied Physics Letters, 2008, 92(15): 151107

16. Seifert T, Jaiswal S, Martens U, Hannegan J, Braun L, Maldonado P, Freimuth F, Kronenberg A, Henrizi J, Radu I, Beaurepaire E, Mokrousov Y, Oppeneer P M, Jourdan M, Jakob G, Turchinovich D, Hayden L M, Wolf M, Münzenberg M, Kläui M, Kampfrath T. Efficient metallic spintronic emitters of ultrabroadband terahertz radiation. Nature Photonics, 2016, 10(7): 483–488

17. Clough B, Dai J, Zhang X C. Laser air photonics: beyond the terahertz gap. Materials Today, 2012, 15(1-2): 50–58

18. Chen Y, Yamaguchi M, Wang M, Zhang X C. Terahertz pulse generation from noble gases. Applied Physics Letters, 2007, 91 (25): 251116

19. Lu X, Karpowicz N, Chen Y, Zhang X C. Systematic study of broadband terahertz gas sensor. Applied Physics Letters, 2008, 93 (26): 261106

20. Kress M, Löffler T, Eden S, Thomson M, Roskos H G. Terahertz-pulse generation by photoionization of air with laser pulses composed of both fundamental and second-harmonic waves. Optics Letters, 2004, 29(10): 1120–1122

21. Xie X, Dai J, Zhang X C. Coherent control of THz wave generation in ambient air. Physical Review Letters, 2006, 96(7): 075005

22. Leisawitz D T, Danchi W C, DiPirro M J, Feinberg L D, Gezari D Y, Hagopian M, Langer W D, Mather J C, Moseley S H, Shao M, Silverberg R F, Staguhn J G, Swain M R, Yorke H W, Zhang X L. Scientific motivation and technology requirements for the SPIRIT and SPECS far-infrared/submillimeter space interferometers. In: Proceedings of SPIE 4013, UV, Optical, and IR Space Telescopes and Instruments. Munich, Germany: SPIE, 2000, 36–46

23. Ferguson B, Zhang X C. Materials for terahertz science and technology. Nature Materials, 2002, 1(1): 26–33

24. Siegel P H. Terahertz technology. IEEE Transactions on Microwave Theory and Techniques, 2002, 50(3): 910–928

25. Tonouchi M. Cutting-edge terahertz technology. Nature Photonics, 2007, 1(2): 97–105

26. Kimmitt M F. Restrahlen to T-rays – 100 years of terahertz radiation. Journal of Biological Physics, 2003, 29(2–3): 77–85

27. Siegel P H. Terahertz pioneer: David H. Auston. IEEE Transactions on Terahertz Science and Technology, 2011, 1(1): 6–8

28. Siegel P H. Terahertz pioneer: Maurice F. Kimmitt 'A Person Who Makes Things Work'. IEEE Transactions on Terahertz Science and Technology, 2012, 2(1): 6–9

29. Siegel P H. Terahertz pioneer: Thomas G. Phillips 'The Sky Above, the Mountain Below'. IEEE Transactions on Terahertz Science and Technology, 2012, 2(5): 478–484

30. Siegel P H. Terahertz pioneer: Frank C. De Lucia 'The Numbers Count'. IEEE Transactions on Terahertz Science and Technology, 2012, 2(6): 578–583

31. Siegel P H. Terahertz pioneer: Richard J. Saykally – water, water everywhere..... IEEE Transactions on Terahertz Science and Technology, 2012, 2(3): 266–270

32. Siegel P H. Terahertz pioneer: Robert W. Wilson the foundations of THz radio science. IEEE Transactions on Terahertz Science and Technology, 2012, 2(2): 162–166

33. Siegel P H. Terahertz pioneer: Daniel R. Grischkowsky 'We Search for Truth and Beauty'. IEEE Transactions on Terahertz Science and Technology, 2012, 2(4): 378–382

34. Siegel P H. Terahertz pioneers: Manfred Winnewisser and Brenda PrudenWinnewisser: 'Equating Hamiltonians to nature'. IEEE Transactions on Terahertz Science and Technology, 2013, 3(3): 229–236

35. Siegel P H. Terahertz pioneer: Sir John B. Pendry 'Theoretical Physics for a Practical World'. IEEE Transactions on Terahertz Science and Technology, 2013, 3(6): 693–701

36. Siegel P H. Terahertz pioneer: Philippe Goy "If You Agree with the Majority, You Might be Wrong". IEEE Transactions on Terahertz Science and Technology, 2013, 3(4): 348–353

37. Siegel P H. Terahertz pioneer: Federico Capasso "Physics by Design: Engineering Our Way Out of the THz Gap". IEEE Transactions on Terahertz Science and Technology, 2013, 3(1): 6–13

38. Siegel P H. Terahertz pioneer: Fritz Keilmann- 'RF Biophysics: From strong field to near field'. IEEE Transactions on Terahertz Science and Technology, 2013, 3(5): 506–514

39. Siegel P H. Terahertz pioneer: Koji Mizuno '50 Years in Submillimeter-Waves: From Otaku to Sensei'. IEEE Transactions on Terahertz Science and Technology, 2013, 3(2): 130–133

40. Siegel P H. Terahertz pioneer: Erik L. Kollberg 'Instrument Maker to the Stars'. IEEE Transactions on Terahertz Science and Technology, 2014, 4(5): 538–544

41. Siegel P H. Terahertz pioneer: Michael Bass 'The THz Light at the End of the Tunnel'. IEEE Transactions on Terahertz Science and Technology, 2014, 4(4): 410–417

42. Siegel P H. Terahertz pioneer: Shenggang Liu 'China's Father of Vacuum and Microwave Electronics'. IEEE Transactions on Terahertz Science and Technology, 2014, 4(1): 6–11

43. Siegel P H. Terahertz pioneer: Mattheus (Thijs) de Graauw 'Intention, Attention, Execution'. IEEE Transactions on Terahertz Science and Technology, 2014, 4(2): 138–146

44. Siegel P H. Terahertz pioneer: Robert J. Mattauch "Two Terminals Will Suffice". IEEE Transactions on Terahertz Science and Technology, 2014, 4(6): 646–652

45. Siegel P H. Terahertz pioneer: Tatsuo Itoh 'Transmission Lines and Antennas: Left and Right'. IEEE Transactions on Terahertz Science and Technology, 2014, 4(3): 298–306

46. Siegel P H. Terahertz pioneer: Xi-Cheng Zhang 'The Face of THz'. IEEE Transactions on Terahertz Science and Technology, 2015, 5(5): 706–714

47. Phillips T G, Keene J. Submillimeter astronomy (heterodyne spectroscopy). Proceedings of the IEEE, 1992, 80(11): 1662–1678

48. Siegel P H, Pikov V. Impact of low intensity millimetre waves on cell functions. Electronics Letters, 2010, 46(26): S70

49. Alexandrov B S, Gelev V, Bishop A R, Usheva A, Rasmussen K O. DNA breathing dynamics in the presence of a terahertz field. Physics Letters A, 2010, 374(10): 1214–1217

50. Yang Y, Mandehgar M, Grischkowsky D R. Broadband THz pulse transmission through the atmosphere. IEEE Transactions on Terahertz Science and Technology, 2011, 1(1): 264–273

51. Svelto O, Hanna D C. Principles of Lasers. Boston, MA: Springer, 2009

52. Wu Z, Fisher A S, Goodfellow J, Fuchs M, Daranciang D, Hogan M, Loos H, Lindenberg A. Intense terahertz pulses from SLAC electron beams using coherent transition radiation. Review of Scientific Instruments, 2013, 84(2): 022701

53. Elias L R, Hu J, Ramian G. The UCSB electrostatic accelerator free electron laser: first operation. Nuclear Instruments & Methods in Physics Research. Section A, Accelerators, Spectrometers, Detectors and Associated Equipment, 1985, 237(1-2): 203–206

54. Reimann K. Table-top sources of ultrashort THz pulses. Reports on Progress in Physics, 2007, 70(10): 1597–1632

55. Kitaeva G K. Terahertz generation by means of optical lasers. Laser Physics Letters, 2008, 5(8): 559–576

56. Hebling J, Yeh K L, Hoffmann M C, Bartal B, Nelson K A. Generation of high-power terahertz pulses by tilted-pulse-front excitation and their application possibilities. Journal of the Optical Society of America. B, Optical Physics, 2008, 25(7): B6

57. Rice A, Jin Y, Ma X F, Zhang X C, Bliss D, Larkin J, Alexander M. Terahertz optical rectification from ⟨110⟩ zinc-blende crystals. Applied Physics Letters, 1994, 64(11): 1324–1326

58. Fülöp J A, Pálfalvi L, Klingebiel S, Almási G, Krausz F, Karsch S, Hebling J. Generation of sub-mJ terahertz pulses by optical rectification. Optics Letters, 2012, 37(4): 557–559

59. Shalaby M, Hauri C P. Demonstration of a low-frequency three-dimensional terahertz bullet with extreme brightness. Nature Communications, 2015, 6(1): 5976

60. Hirori H, Doi A, Blanchard F, Tanaka K. Single-cycle terahertz pulses with amplitudes exceeding 1 MV/cm generated by optical rectification in LiNbO$_3$. Applied Physics Letters, 2011, 98(9): 091106

61. Auston D H. Picosecond optoelectronic switching and gating in silicon. Applied Physics Letters, 1975, 26(3): 101–103

62. Mourou G, Stancampiano C V, Antonetti A, Orszag A. Picosecond microwave pulses generated with a subpicosecond laser-driven semiconductor switch. Applied Physics Letters, 1981, 39(4): 295–296

63. Budiarto E, Margolies J, Jeong S, Son J, Bokor J. High-intensity terahertz pulses at 1-kHz repetition rate. IEEE Journal of Quantum Electronics, 1996, 32(10): 1839–1846

64. Look D C. Molecular beam epitaxial GaAs grown at low temperatures. Thin Solid Films, 1993, 231(1-2): 61–73

65. Beard M C, Turner G M, Schmuttenmaer C A. Subpicosecond carrier dynamics in low-temperature grown GaAs as measured by time-resolved terahertz spectroscopy. Journal of Applied Physics, 2001, 90(12): 5915–5923

66. Richards P L. Bolometers for infrared and millimeter waves. Journal of Applied Physics, 1994, 76(1): 1–24

67. Mauskopf P D, Bock J J, Del Castillo H, Holzapfel W L, Lange A E. Composite infrared bolometers with Si$_3$N$_4$ micromesh absorbers. Applied Optics, 1997, 36(4): 765–771

68. Nahum M, Martinis J M. Ultrasensitive-hot-electron microbolometer. Applied Physics Letters, 1993, 63(22): 3075–3077

69. Golay M J E. A pneumatic infra-red detector. Review of Scientific Instruments, 1947, 18(5): 357–362

70. Gautschi G. Piezoelectric Sensorics: Force, Strain, Pressure, Acceleration and Acoustic Emission Sensors, Materials and Amplifiers. Berlin, Heidelberg: Springer, 2002

71. Komiyama S, Astafiev O, Antonov V, Kutsuwa T, Hirai H. A single-photon detector in the far-infrared range. Nature, 2000, 403(6768): 405–407

72. Kim K T, Zhang C, Shiner A D, Schmidt B E, Légaré F, Villeneuve D M, Corkum P B. Petahertz optical oscilloscope. Nature Photonics, 2013, 7(12): 958–962

73. Teo S M, Ofori-Okai B K, Werley C A, Nelson K A. Single-shot THz detection techniques optimized for multidimensional THz spectroscopy. Review of Scientific Instruments, 2015, 86(5): 051301

74. Wu Q, Zhang X C. Free-space electro-optic sampling of terahertz beams. Applied Physics Letters, 1995, 67(24): 3523–3525

75. Leitenstorfer A, Hunsche S, Shah J, Nuss M C, Knox W H. Detectors and sources for ultrabroadband electro-optic sampling: experiment and theory. Applied Physics Letters, 1999, 74(11): 1516–1518

76. Auston D H, Smith P R. Generation and detection of millimeter waves by picosecond photoconductivity. Applied Physics Letters, 1983, 43(7): 631–633

77. Grischkowsky D, Keiding S, van Exter M, Fattinger C. Far-infrared time-domain spectroscopy with terahertz beams of dielectrics and semiconductors. Journal of the Optical Society of America. B, Optical Physics, 1990, 7(10): 2006

78. Wu Q, Hewitt T D, Zhang X C. Two-dimensional electro-optic imaging of THz beams. Applied Physics Letters, 1996, 69(8): 1026–1028

79. Mittleman D M, Jacobsen R H, Nuss M C. T-ray imaging. IEEE Journal of Selected Topics in Quantum Electronics, 1996, 2(3): 679–692

80. Mittleman D M, Hunsche S, Boivin L, Nuss M C. T-ray tomography. Optics Letters, 1997, 22(12): 904–906

81. Woodward R M, Cole B E, Wallace V P, Pye R J, Arnone D D, Linfield E H, Pepper M. Terahertz pulse imaging in reflection geometry of human skin cancer and skin tissue. Physics in Medicine and Biology, 2002, 47(21): 3853–3863

82. Seco-Martorell C, López-Domínguez V, Arauz-Garofalo G, Redo-Sanchez A, Palacios J, Tejada J. Goya's artwork imaging with Terahertz waves. Optics Express, 2013, 21(15): 17800–17805

83. Zhong H, Xu J Z, Xie X, Yuan T, Reightler R, Madaras E, Zhang X C. Nondestructive defect identification with terahertz time-of-flight tomography. IEEE Sensors Journal, 2005, 5(2): 203–208

84. Beard M C, Turner G M, Schmuttenmaer C A. Terahertz Spectroscopy. Journal of Physical Chemistry B, 2002, 106(29): 7146–7159

85. Sell A, Leitenstorfer A, Huber R. Phase-locked generation and field-resolved detection of widely tunable terahertz pulses with amplitudes exceeding 100 MV/cm. Optics Letters, 2008, 33(23): 2767–2769

86. Kampfrath T, Tanaka K, Nelson K A. Resonant and nonresonant control over matter and light by intense terahertz transients. Nature Photonics, 2013, 7(9): 680–690

87. Schubert O, Hohenleutner M, Langer F, Urbanek B, Lange C, Huttner U, Golde D, Meier T, Kira M, Koch S W, Huber R. Sub-cycle control of terahertz high-harmonic generation by dynamical Bloch oscillations. Nature Photonics, 2014, 8(2): 119–123

88. Hamster H, Sullivan A, Gordon S, White W, Falcone R W. Subpicosecond, electromagnetic pulses from intense laser-plasma interaction. Physical Review Letters, 1993, 71(17): 2725–2728

89. Löffler T, Jacob F, Roskos H G. Generation of terahertz pulses by photoionization of electrically biased air. Applied Physics Letters, 2000, 77(3): 453–455

90. Cook D J, Hochstrasser R M. Intense terahertz pulses by four-wave rectification in air. Optics Letters, 2000, 25(16): 1210–1212

91. Liu J, Zhang X C. Terahertz-radiation-enhanced emission of fluorescence from gas plasma. Physical Review Letters, 2009, 103(23): 235002

92. Clough B, Liu J, Zhang X C. Laser-induced photoacoustics influenced by single-cycle terahertz radiation. Optics Letters, 2010, 35(21): 3544–3546

93. Hamster H, Sullivan A, Gordon S, Falcone R W. Short-pulse terahertz radiation from high-intensity-laser-produced plasmas. Physical Review E: Statistical Physics, Plasmas, Fluids, and Related Interdisciplinary Topics, 1994, 49(1): 671–677

94. Durand M, Houard A, Prade B, Mysyrowicz A, Durécu A, Moreau B, Fleury D, Vasseur O, Borchert H, Diener K, Schmitt R, Théberge F, Chateauneuf M, Daigle J F, Dubois J. Kilometer range filamentation. Optics Express, 2013, 21(22): 26836–26845

95. D'Amico C, Houard A, Franco M, Prade B, Mysyrowicz A, Couairon A, Tikhonchuk V T. Conical forward THz emission from femtosecond-laser-beam filamentation in air. Physical Review Letters, 2007, 98(23): 235002

96. Houard A, Liu Y, Prade B, Tikhonchuk V T, Mysyrowicz A. Strong enhancement of terahertz radiation from laser filaments in air by a static electric field. Physical Review Letters, 2008, 100(25): 255006

97. Liu Y, Houard A, Prade B, Mysyrowicz A, Diaw A, Tikhonchuk V T. Amplification of transition-Cherenkov terahertz radiation of femtosecond filament in air. Applied Physics Letters, 2008, 93(5): 051108

98. Mitryukovskiy S I, Liu Y, Prade B, Houard A, Mysyrowicz A. Coherent synthesis of terahertz radiation from femtosecond laser filaments in air. Applied Physics Letters, 2013, 102(22): 221107

99. Kim K Y, Glownia J H, Taylor A J, Rodriguez G. Terahertz emission from ultrafast ionizing air in symmetry-broken laser fields. Optics Express, 2007, 15(8): 4577–4584

100. Karpowicz N, Zhang X C. Coherent terahertz echo of tunnel ionization in gases. Physical Review Letters, 2009, 102(9): 093001

101. Bergé L, Skupin S, Köhler C, Babushkin I, Herrmann J. 3D numerical simulations of THz generation by two-color laser filaments. Physical Review Letters, 2013, 110(7): 073901

102. Clerici M, Peccianti M, Schmidt B E, Caspani L, Shalaby M, Giguère M, Lotti A, Couairon A, Légaré F, Ozaki T, Faccio D, Morandotti R. Wavelength scaling of terahertz generation by gas ionization. Physical Review Letters, 2013, 110(25): 253901

103. Oh T I, Yoo Y J, You Y S, Kim K Y. Generation of strong terahertz fields exceeding 8 MV/cm at 1 kHz and real-time beam profiling. Applied Physics Letters, 2014, 105(4): 041103

104. Thomson M D, Blank V, Roskos H G. Terahertz white-light pulses from an air plasma photo-induced by incommensurate two-color optical fields. Optics Express, 2010, 18(22): 23173–23182

105. Dai J, Zhang X C. Terahertz wave generation from gas plasma using a phase compensator with attosecond phase-control accuracy. Applied Physics Letters, 2009, 94(2): 021117

106. Wen H, Lindenberg A M. Coherent terahertz polarization control through manipulation of electron trajectories. Physical Review Letters, 2009, 103(2): 023902

107. Dai J, Karpowicz N, Zhang X C. Coherent polarization control of terahertz waves generated from two-color laser-induced gas plasma. Physical Review Letters, 2009, 103(2): 023001

108. Zhong H, Karpowicz N, Zhang X C. Terahertz emission profile from laser-induced air plasma. Applied Physics Letters, 2006, 88(26): 261103

109. Klarskov P, Strikwerda A C, Iwaszczuk K, Jepsen P U. Experimental three-dimensional beam profiling and modeling of a terahertz beam generated from a two-color air plasma. New Journal of Physics, 2013, 15(7): 075012

110. Blank V, Thomson M D, Roskos H G. Spatio-spectral character-istics of ultra-broadband THz emission from two-colourphotoex-cited gas plasmas and their impact for nonlinear spectroscopy. New Journal of Physics, 2013, 15(7): 075023

111. You Y S, Oh T I, Kim K Y. Off-axis phase-matched terahertz emission from two-color laser-induced plasma filaments. Physical Review Letters, 2012, 109(18): 183902

112. Gorodetsky A, Koulouklidis A D, Massaouti M, Tzortzakis S. Physics of the conical broadband terahertz emission from two-color laser-induced plasma filaments. Physical Review A., 2014, 89(3): 033838

113. Wang T J, Yuan S, Chen Y, Daigle J F, Marceau C, Théberge F,

Châteauneuf M, Dubois J, Chin S L. Toward remote high energy terahertz generation. Applied Physics Letters, 2010, 97(11): 111108

114. Wang T J, Daigle J F, Yuan S, Théberge F, Châteauneuf M, Dubois J, Roy G, Zeng H, Chin S L. Remote generation of high-energy terahertz pulses from two-color femtosecond laser filamentation in air. Physical Review A., 2011, 83(5): 053801

115. Nahata A, Heinz T F. Detection of freely propagating terahertz radiation by use of optical second-harmonic generation. Optics Letters, 1998, 23(1): 67–69

116. Liu J, Zhang X C. Enhancement of laser-induced fluorescence by intense terahertz pulses in gases. IEEE Journal of Selected Topics in Quantum Electronics, 2011, 17(1): 229–236

117. Liu J, Dai J, Zhang X C. Ultrafast broadband terahertz waveform measurement utilizing ultraviolet plasma photoemission. Journal of the Optical Society of America B, Optical Physics, 2011, 28(4): 796

118. Liu J, Dai J, Chin S L, Zhang X C. Broadband terahertz wave remote sensing using coherent manipulation of fluorescence from asymmetrically ionized gases. Nature Photonics, 2010, 4(9): 627–631

119. Clough B, Liu J, Zhang X C. "All air-plasma" terahertz spectroscopy. Optics Letters, 2011, 36(13): 2399–2401

120. Maker P D, Terhune R W, Savage C M. Optical third harmonic generation. In: Proceedings of the 3rd International Congress, Quantum Electron. Paris: Dunod Éditeur, 1964, 1559

121. Talebpour A, Yang J, Chin S L. Semi-empirical model for the rate of tunnel ionization of N_2 and O_2 molecule in an intense Ti: sapphire laser pulse. Optics Communications, 1999, 163(1-3): 29–32

122. Couairon A, Mysyrowicz A. Femtosecond filamentation in transparent media. Physics Reports, 2007, 441(2-4): 47–189

123. Chin S L. Femtosecond Laser Filamentation. New York: Springer, 2010

124. Abdollahpour D, Suntsov S, Papazoglou D G, Tzortzakis S. Measuring easily electron plasma densities in gases produced by ultrashort lasers and filaments. Optics Express, 2011, 19(18): 16866–16871

125. Arévalo E, Becker A. Theoretical analysis of fluorescence signals in filamentation of femtosecond laser pulses in nitrogen molecular gas. Physical Review A., 2005, 72(4): 043807

126. Talebpour A, Petit S, Chin S. Re-focusing during the propagation of a focused femtosecond Ti:Sapphire laser pulse in air. Optics Communications, 1999, 171(4-6): 285–290

127. Bukin V V, Vorob'ev N S, Garnov S V, Konov V I, Lozovoi V I, Malyutin A A, Shchelev M Y, Yatskovskii I S. Formation and development dynamics of femtosecond laser microplasma in gases. Quantum Electronics, 2006, 36(7): 638–645

128. Martin F, Mawassi R, Vidal F, Gallimberti I, Comtois D, Pépin H, Kieffer J C, Mercure H P. Spectroscopic study of ultrashort pulse laser-breakdown plasmas in air. Applied Spectroscopy, 2002, 56 (11): 1444–1452

129. Herzberg G. Molecular Spectra and Molecular Structure. Malabar, FL: R.E. Krieger Pub. Co, 1989

130. Becker A, Bandrauk A D, Chin S L. S-matrix analysis of non-resonant multiphoton ionisation of inner-valence electrons of the nitrogen molecule. Chemical Physics Letters, 2001, 343(3-4): 345–350

131. Xu H L, Azarm A, Bernhardt J, Kamali Y, Chin S L. The mechanism of nitrogen fluorescence inside a femtosecond laser filament in air. Chemical Physics, 2009, 360(1-3): 171–175

132. Vidal F, Comtois D, Chien C Y, Desparois A, La Fontaine B, Johnston T W, Kieffer J C, Mercure H P, Pepin H, Rizk F A. Modeling the triggering of streamers in air by ultrashort laser pulses. IEEE Transactions on Plasma Science, 2000, 28(2): 418–433

133. Sato M, Higuchi T, Kanda N, Konishi K, Yoshioka K, Suzuki T, Misawa K, Kuwata-Gonokami M. Terahertz polarization pulse shaping with arbitrary field control. Nature Photonics, 2013, 7(9): 724–731

134. Amico C D, Houard A, Akturk S, Liu Y, Le Bloas J, Franco M, Prade B, Couairon A, Tikhonchuk V T, Mysyrowicz A. Forward THz radiation emission by femtosecond filamentation in gases: theory and experiment. New Journal of Physics, 2008, 10(1): 013015

Fabrizio Buccheri graduated from University of Palermo with a Bachelor of Engineering and a Master of Engineering in Electronics Engineering in November 2007 and November 2010 respectively, both with full marks and honor. His undergraduate thesis project with the title "Optical Biosensor based on Surface Plasmon Resonance for Wine Quality Control" won the first prize as best undergraduate project at the regional level. In 2010, Fabrizio was awarded a research internship from the Institut National de la Recherche Scientifique in Varennes, Canada, under the supervision of Prof. R. Morandotti. In Canada, Fabrizio developed his experimental master thesis project with the title "Terahertz Time Domain Spectroscopy with Subwavelength Spatial Resolution." In 2011, Fabrizio is awarded a Fulbright scholarship to support the pursuit of his PhD degree in the United States. He joined Prof. X.-C. Zhang's research group in Rensselaer Polytechnic Institute and then followed him to University of Rochester, The Institute of Optics. In 2016, he was awarded the Best Graduate Student Project from The Institute of Optics by Rochester Precision Optics. Fabrizio is an active member of the professional associations OSA and SPIE.

Fabrizio currently works for Prysmian Group designing the next generation monitoring systems for the energy industry.

Email: fbuccheri@fulbrightmail.org

Pingjie Huang is an associate professor in the State Key Laboratory of Industrial Control Technology, College of Control Science and Engineering, Zhejiang University (ZJU). He received his Ph.D. degree in mechanical engineering, with specialty in information sensing and instrumentation from Zhejiang University in 2004 and obtained his B.Sc. and M.Sc. degrees

from Huazhong Agricultural University in 1996 and Xi'an University of Technology in 1999, respectively. His research interests mainly focus on advanced transducer and measurement, process and environmental information processing and event detection, and computer control system design and development, etc. He is a key member of the research group in Zhejiang University for early warning techniques and systems for urban water quality assurance, NDT&E of conductive structures, food products, water samples, and bio-tissue etc. base on THz-TDS, UV-Vis, and ECT methods. In these five years, he has authored/co-authored more than 40 peer-reviewed papers and conference papers.

Supported by the CSC and starting from September 2017 for a period of one year, Pingjie Huang is a visiting scholar in Prof. Xi-Cheng Zhang's research group in The Institute of Optics, University of Rochester working on terahertz science and technology.

Email: huangpingjie@zju.edu.cn

Xi-Cheng Zhang, Parker Givens Chair of Optics, was Director of The Institute of Optics, University of Rochester (UR), NY, a foremost institution in optics and optical physics research and education (Jan. 2012 – Jun. 2017). Prior to joining UR, he pioneered world-leading research in the field of ultrafast laser-based terahertz technology and optical physics at Rensselaer Polytechnic Institute (RPI), Troy NY ('92-'12). At RPI, he is the Eric Jonsson Professor of Science; Acting Head at the Department of Physics, Applied Physics & Astronomy; Professor of Electrical, Computer & System; and Founding Director of the Center for THz Research. He is co-founder of Zomega Terahertz Corp. With a B.S. degree ('82) from Peking University, he earned the M.S. ('83) and Ph.D. ('86) degrees in Physics from Brown University, RI.

Dr. Zhang served as Editor-in-Chief of *Optics Letters*, OSA ('14–'19). He is a Fellow of AAAS, APS, IEEE, OSA, and SPIE. Previous positions included visiting scientist at MIT ('85), Physical Tech. Division of Amoco Research Center ('87), EE Dept. at Columbia University ('87–'91); Distinguished Visiting Scientist at Jet Propulsion Laboratory, Caltech (2006). He holds 29 US patents, and is a prolific author and speaker.

His honors and awards include: Humboldt Prize '18); Australian Academy of Science Selby Fellow ('17); IRMMW-THz Kenneth Button Prize ('14); OSA William F. Meggers Award ('12); IEEE Photonics Society William Streifer Scientific Achievement Award ('11); Rensselaer William H. Wiley 1866 Award ('09); Japan Society for the Promotion of Science Fellowship & NRC-CIAR Distinguished Visiting Scientist, Canada ('04); First Heinrich Rudolf Hertz Lecturer, RWTH, Aachen, Germany ('03). He also served two years as a Distinguished Lecturer of IEEE/LEOS. He received Rensselaer Early Career Award ('96), Research Corporation Cottrell Scholar Award ('95), NSF Early Career Award ('95), K.C. Wong Prize, K.C. Wong Foundation, Hong Kong ('95), NSF Research Initiation Award ('92). In '93–'94, he was an AFOSR-SRPF Fellow at Hanscom Air Force Base.

Email: xi-cheng.zhang@rochester.edu